Cu and Zn isotope fractionation during extreme chemical weathering

Susan H. Little[1,2]*, Sophie Munson[2], Julie Prytulak[3], Barry J. Coles[2], Samantha J. Hammond[4], Mike Widdowson[5]

1. Department of Earth Sciences, University College London, Gower Place, London, WC1E 6BS, UK.

    *susan.little@ucl.ac.uk

2. Department of Earth Science and Engineering, Royal School of Mines, Imperial College London, London, SW7 2BP, UK.

3. Department of Earth Sciences, Durham University, Durham DH1 3LE, UK.

4. Department of Environment, Earth and Ecosystems, The Open University, Walton Hall, Milton Keynes, MK7 6AA, UK.

5. School of Environmental Sciences, Cohen Building, University of Hull, Hull, HU6 7RX, UK.

23 July 2019

For resubmission to *Geochimica et Cosmochimica Acta*

Abstract

Copper and Zn are trace metal micronutrients whose stable isotope systematics are receiving increasing attention as possible paleoenvironmental tracers. However, to realise this potential, their behaviour during chemical weathering must be better constrained. We present coupled Cu and Zn isotope data for a well-characterised Indian laterite weathering profile, which includes a full suite of samples from unaltered greywacke bedrock to indurated lateritic duricrust. This sample set provides an exceptional opportunity to interrogate Cu and Zn isotope compositions during an extreme example of chemical weathering. Despite their occurrence in different host phases within the parent greywacke, Cu and Zn isotopes behave coherently during weathering. We observe preferential loss of heavy isotopes at increasing degrees of alteration, with 0.6‰ total variability in $\delta^{66}Zn$ and 0.9‰ in $\delta^{65}Cu$. Given the absence of evidence for CuS or ZnS phases in the parent lithology, we attribute the liberation of heavy isotopes to organic complexation in the aqueous phase and/or incorporation of light isotopes in secondary aluminous Fe-oxides. Strong enrichment of both metals is also associated with a peak in Mn at a previously identified paleo-water table horizon. This dataset confirms that weathering under oxygenated conditions releases isotopically heavy Cu, regardless of the host phase. Meanwhile, Zn isotopes are only fractionated to any significant extent at the most extreme degrees of chemical weathering reached during lateritization. We conclude that the isotopic composition of the weathering-derived input of Zn to rivers should be largely insensitive to climate change on geological timescales.

Keywords: Cu, Zn, Isotopes, Laterite, Weathering, Organic complexation, Fe oxides

1.0 Introduction

Variations in the stable isotope ratios of the bioessential transition metals Zn and Cu are increasingly being utilised as tracers of past Earth surface processes, particularly in the ocean (e.g., Kunzmann et al., 2013; Pons et al., 2013; Chi Fru et al., 2016; John et al., 2017; Isson et al., 2018). However, while isotopic shifts in sedimentary records of both Zn and Cu are undoubtedly present during periods of global change (e.g., Snowball Earth events in the Neoproterozoic), and often tantalisingly systematic (e.g., Kunzmann et al., 2013; John et al., 2017), their underlying controls remain difficult to elucidate.

Paleoceanographic interpretations of observed Zn and Cu isotope variations can be divided into one or more of three main causal categories. (1) Invoking a change in biological productivity (or other related process) in the ocean itself (Kunzmann et al., 2013; Isson et al., 2018). (2) Suggesting a change in the balance of the removal fluxes to different oceanic sinks, for example, due to a change in ocean redox state (Chi Fru et al., 2016; John et al., 2017). (3) Interpretations that require a change in the magnitude or isotopic composition of a *source* of the element to the ocean, for example, a change in the weathering-derived flux due to tectonic or climate change (Kunzmann et al., 2013; Pons et al., 2013; Chi Fru et al., 2016).

Weathering of the continents supplies solutes to rivers, which constitute a key input of Zn and Cu to the modern ocean (Little et al., 2014b). The Zn and Cu isotope composition of rivers will thus reflect that supplied by weathering, though biogeochemical processes in rivers may subsequently modify this primary signature (e.g., Borrok et al., 2008; Coutaud et al., 2014; Szynkiewicz and Borrok, 2016; Coutaud et al., 2018). The aim of this study is to investigate Zn and Cu isotope fractionation during extreme chemical weathering. This approach provides an end-member constraint on the degree of isotope fractionation possible in the weathering environment. It is a starting point from which to evaluate the leverage of chemical weathering in modifying the isotopic composition of rivers through time, and hence its possible influence on the wider marine inventory.

33

34 A study of the dissolved phase in rivers found a discharge-weighted Zn isotope

35 composition unfractionated from continental rocks (Little et al., 2014b). The absence

36 of systematic Zn isotope fractionation in rivers implies little or no Zn isotope

37 fractionation during weathering, a hypothesis partially supported by studies of Zn

38 isotopes in soils (Bigalke et al., 2010a; Vance et al., 2016; Opfergelt et al., 2017; Suhr

39 et al., 2018). However, studies carried out in extreme, (sub-) tropical weathering

40 regimes have observed preferential release of heavy Zn isotopes (Viers et al., 2007;

41 Lv et al., 2016; Guinoiseau et al., 2017; Suhr et al., 2018). This observation has been

42 explained by various processes, including release of isotopically heavy Zn during

43 oxidative weathering of sulphides (Fernandez and Borrok, 2009; Lv et al., 2016);

44 organic complexation of the heavy isotope in the dissolved pool (Guinoiseau et al.,

45 2017); incorporation or adsorption of isotopically light Zn in/on clays (Viers et al.,

46 2007; Guinoiseau et al., 2017) or Fe oxides (Viers et al., 2007; Suhr et al., 2018); or

47 release of isotopically light Zn from refractory mineral phases and subsequent re-

48 precipitation with Fe oxide phases (Suhr et al., 2018).

49

50 In contrast to Zn, Cu in the riverine dissolved pool is isotopically heavy relative to

51 rocks (Vance et al., 2008); this behaviour is similar to observations for Mo (Archer

52 and Vance, 2008; Neubert et al., 2011), Li (Huh et al., 1998), Ni (Cameron and

53 Vance, 2014), and Cr isotopes (Frei et al., 2014). Accordingly, there are two proposed

54 explanations for the heavy Cu isotope composition in rivers: (1) An equilibrium

55 isotope fractionation in rivers (Vance et al., 2008) and/or in soils (Vance et al., 2016)

56 between an isotopically heavy, organic ligand bound, dissolved pool and an

57 isotopically light pool sorbed to particulates; (2) Redox-driven release of isotopically

58 heavy Cu during oxidative weathering of sulphides in black shales or supergene

59 systems (Mathur et al., 2005; Mathur et al., 2012; Mathur and Fantle, 2015; Lv et al.,

60 2016).

61

62 The present study investigates the Zn and Cu isotope systematics of a well-

63 characterised Indian lateritic weathering profile. The term laterite is not always used

64 ubiquitously or consistently. We follow the definition in the widely cited

65 *Encyclopaedia of Geomorphology* (Goudie, 2004; Widdowson, 2004), which states

66 that: 'Laterite is an iron-rich, sub-aerial, weathering product, commonly believed to

evolve as a result of intense, *in situ* substrate alteration under tropical or sub-tropical climatic conditions.' A lateritic weathering profile therefore constitutes a chemical residuum resulting from the relative enrichment of relatively immobile elements (notably Fe and Al), as described initially by Newbold (1844), and more recently by many other authorities (e.g., McFarlane, 1976; McFarlane, 1983; Schellman, 1983; Aleva, 1984; Widdowson, 2004, 2007; Babechuk et al., 2014). This definition emphasises the relative enrichment of Fe (and Al) through desilication processes involved in the development of a laterite profile; this enrichment/depletion may be modified through hydromorphism associated with oscillating redox conditions in the developing weathering profile and typically driven by pluvial seasonality and associated water-table recharge.

Laterites typically form on parent lithologies with inherently high iron contents (such as mafic and ultramafic igneous rocks and chemically immature sediments) and on stable continental landmasses subject to high mean annual temperatures, high humidity and seasonal, high annual rainfall (Widdowson, 2007). These climatic conditions promote intense *in situ* chemical weathering and mineral alteration, making laterites an ideal natural laboratory to study the weathering process *in extremis*. Today, laterites and associated weathering products account for approximately 30% of Earth surface cover, and almost 50% of continental drainage flows over these terrains (Tardy, 1997).

To date, two studies have reported Zn isotope data from lateritic weathering profiles, one developed on granodiorite in Cameroon (Viers et al., 2007) and the other for the Bidar laterite developed on Deccan basalt in central India (Suhr et al., 2018). Both studies observe preferential retention of light Zn isotopes in the laterite residues. To the best of our knowledge, no Cu isotope data for laterites has yet been reported.

2.0 Geological setting and background

2.1 Geological setting

The coastal lowlands of western peninsular India between ~8° and ~19°N comprise dissected, laterite-capped 'tablelands' with maximum altitudes of ~150–200m in the east systematically descending to less than 50–100m at the coastline (Widdowson, 2009). These tablelands are remnants of a once extensive laterite belt that extended along the length of western peninsular India (Widdowson, 2009), developed upon a variety of lithologies. This belt provides evidence of an important phase of Cenozoic lateritization that affected western India during the latest Eocene to the Miocene (Schmidt et al., 1983; Bonnet et al., 2014), when climatic conditions were optimal for deep weathering (Tardy et al., 1991).

The site of the investigated profile lies in the small coastal state of Goa. Metamorphic rocks of varying grade and composition dominate the geology of Goa (Pascoe, 1950) and include weakly metamorphosed Dharwar sediments of the Dharwar craton, including abundant Late Archaean greywackes (Argast and Donnelly, 1986; Devaraju et al., 2010; Dessai, 2011). The samples in this study (hereafter referred to as 'SQ') are from a quarried laterite profile developed upon meta-greywackes of the Sanvordem Fm (of the Proterozoic age Dharwar Supergroup; > 2.5 Ga) at Merces village, near Panjim Goa (15°28'44"N, 73°52'35"E; Fig. 1).

The parent greywacke consists of a detrital assemblage of quartz, feldspar and volcanic rock fragments (Srinivasan et al., 1989) and geochemical analysis suggests that the bulk sediment was derived from submarine weathering of a felsic volcanic source (Devaraju et al., 2010). Sparse biotite has developed in response to low-grade thermal metamorphism of unknown age. The SQ laterite profile itself is of probable Oligocene-Miocene age (c. 35 – 20 Ma; Schmidt et al., 1983; Bonnet et al., 2014), and developed upon the low-lying coastal (Konkan) plain, subsequent to erosion (i.e. removal of c.1 – 1.5km thickness) across the Indian continental margin (Widdowson, 1997; Widdowson and Gunnell, 1999).

2.2 Sample description

The lithology and mineralogy of the 34 m thick laterite profile has previously been reported in Wimpenny et al. (2007) as the SQ samples series, and comprehensively in Hibbert (2017) as an independent MQ sample series. A schematic diagram of the SQ

profile is shown in Figure 2 (mineralogy and major element data from Wimpenny et
al., 2007). Samples SQ2 – SQ14 were sampled from increasingly shallow depths and
represent a greywacke parent that has undergone increasing degrees of alteration
(Table S1; Figs. 2, 3). Sample SQ1 was taken from a small mafic dyke, which cuts
unaltered greywacke near the base of the profile. All samples have previously been
analyzed for major element (Table S2) and high-precision trace element
concentrations (Table S3) (Howarth et al., 2018; Wimpenny et al., 2007).

Deep lateritic weathering profiles such as the one described here have considerable
antiquity and affect the substratum far below that of modern pedogenetic processes.
The degree of alteration progresses upward from unaltered 'parent' material, through
saprock to saprolite, through a 'mottled zone', and ultimately to the topmost Fe-rich
laterite duricrust (i.e. 'carapace' and then indurated 'cuirasse' in the francophone
terminology).

Saprock (from the Greek '*sapros*' meaning 'rotten') is the first stage of weathering: It
consists of partially weathered minerals and as yet unweathered minerals (e.g.,
feldspars have begun to alter to clay minerals and/or olivine to iddingsite). Saprock
maintains all the fabrics and features of the fresh rock, and is distinguished from the
more advanced stage of saprolite by retaining much of its original physical strength,
and some primary mineralogy. Saprolite is more altered than saprock but, like
saprock, there has been little or no change in bulk volume, and the distribution of
resistant minerals remain more or less in position as they occurred in the parent.
Weatherable minerals in saprolite are typically wholly pseudomorphed by clays
and/or oxides and oxyhydroxides, whilst the original rock fabric remains largely
preserved (Taylor and Eggleton, 2001). In the zone of alternating reduction and
oxidation due to repeated wetting and drying, segregation of iron occurs, forming
'mottles'. The uppermost laterite duricrust hardens irreversibly due to complete
drying and oxic conditions, and consists predominantly of crystallised Fe and Al
oxide and oxyhydroxides.

The SQ profile can be divided into four zones of alteration (Figs. 2, 3), as defined by
Wimpenney et al. (2007):

166   Zone I, at 34 – 15m depth (samples SQ2 – SQ6), exhibits no alteration (parent rock)

167   or low degrees of alteration while retaining the primary texture and fabric of the

168   bedrock (saprock);

169   Zone II, at 15 – 8.5m depth (samples SQ7 – SQ9), consists of altered saprolite in

170   which most weatherable primary minerals are destroyed, then passing into a 'mottled'

171   region, in which secondary minerals and Fe-Al-rich accretions (i.e. mottles) form;

172   Zone III, at 8.5 – 7m depth (samples SQ10 and SQ11), is a narrow zone thought to be

173   influenced by a paleo-water table (Wimpenny et al., 2007);

174   Zone IV, at 7m – surface (samples SQ12 – SQ14), is the Fe-rich cap in which

175   secondary minerals are removed and the Fe-Al-rich accretions fuse to form a resistant,

176   indurated laterite duricrust.

177   The 'line of seepage', at ~15m depth, divides little altered greywacke (zone I) from

178   the zones of increasing alteration above, and is so-called because it marks a

179   significant increase in porosity and permeability (Wimpenny et al., 2007).

180

181   The mineralogical changes that occur upwards in the profile (Table S1, Fig. 3) are

182   reflected in variations in major element concentrations (Table S2, Fig. 2),

183   characterized by a general decrease in Si and concomitant enrichment in Fe and Al

184   (Wimpenny et al., 2007; Widdowson, 2009). In the low alteration zone I, the range of

185   major element concentration variations are somewhat limited (Table S2, Fig. 2) and

186   are likely related to lithological heterogeneity in the parent greywacke (Widdowson,

187   2009). Above the line of seepage, in zones II and IV, there is an increasing degree of

188   depletion of more mobile elements (e.g., Si, Mg, Ca, Na, K), due to the formation and

189   then breakdown and removal of secondary clay minerals, generating the observed

190   enrichment of less mobile elements (e.g., Fe, Al and Ti) in the residue (Widdowson,

191   2009). Notably, this broad pattern is interrupted at ~7 – 8.5m depth (zone III; samples

192   SQ10 and 11) by significantly elevated concentrations of Fe and Mn and depletion of

193   Al; previously interpreted as the depth of a paleo-water table (Fig. 2; Wimpenny et

194   al., 2007).

195

196   Trace element concentrations exhibit similar coherent trends as the rock becomes

197   increasingly altered in zones II-IV (Wimpenny et al., 2007; Howarth et al., 2018).

198   Some fluid-mobile elements (e.g., Li, Rb, Ba, Cu, Zn) show a general decrease in

199   concentration towards the surface but a pronounced peak at the paleo-water table (Fig.

S1A). Other fluid mobile elements, particularly the REE and PGEs, show enrichment
at the paleo-water table and in zone IV (Fig. S1B), this is attributed to mobilization in
low pH, high Eh conditions below, followed by scavenging from solution and
incorporation in the oxide phases that precipitate above (Wimpenny et al., 2007). By
contrast, relatively immobile elements (e.g., Zr, Ti, Nb) display a general increase in
concentration towards the surface and a pronounced concentration decrease at the
paleo-water table (Fig. S1C).

3.0 Analytical Methods

3.1 Sulphur analyses

Sulphur concentrations were measured on an aliquot of solution previously digested
for high precision trace element analysis (see Howarth et al., 2018, for details on
digestion techniques). Analyses were conducted on an Agilent triple quadrupole ICP-
MS (ICP-QQQ) at the Open University. For conventional ICP-MS systems measuring
sulphur concentrations has been challenging, owing to the high background
contribution (from O_2). The ICP-QQQ has an octopole reaction system (ORS) that
separates two quadrupole mass filters, allowing for targeted interference removal. For
S we use O_2 as the reactive gas, forming SO^+ as the product in the ORS, and measure
the mass shifted oxide ion (i.e. at mass 50 for ^{34}S). This effectively reduces the
background from ~1.1 x 10^4 cps to ~2 x 10^2 cps. Detection limits are 0.2 ng/g in the
solutions (equivalent to 0.2 µg/g in the rock – samples are diluted 1000 fold prior to
analysis). Analyses were standardised against a suite of five reference materials
(BIR-1, W-2, BHVO-2, AGV-1, BE-N) measured at the start of each analytical
session. An internal standard solution was also bled in online throughout the
analytical session, and used to monitor and correct for instrument drift. In addition, a
monitor block, consisting of BHVO-2 (digested at Imperial College with the
unknowns and not used in the calibration) BE-N and 2% HNO_3 was run every 4 – 5
unknowns to further monitor drift, and to monitor precision and accuracy of
measurements.

233   The reference materials used in the calibration have only information values listed in

234   the GEOREM database (and where uncertainties are quoted these are also large, e.g

235   BHVO-2 = 164 ± 25 µg/g). However, for the majority of materials we find that using

236   these information values yields a calibration line with an R^2 value of 0.9995. We also

237   find that rock reference materials behave very similarly to the samples during

238   ionisation in the plasma, and therefore find this a more robust method of calibrating

239   rather than having to apply an ionisation correction to a suite of synthetic calibration

240   materials. The one outlier from our calibration line is BIR-1. Further investigation by

241   standard addition methods indicate that the concentration of S is 4.5 µg/g in three

242   further BIR-1 digests from our powder aliquot (rather than 70 µg/g as quoted from

243   GEOREM) and, when this is taken into account, the BIR-1 measurements again sit on

244   the calibration line as described above, and do not alter the R^2 value of the line. We

245   find that our repeat measurements of the BHVO-2 standard digested at Imperial

246   College show both a precision and accuracy of <4 % (RSD) compared to the

247   information values given. Whilst some caution must be exercised in using these

248   information values, we remain confident in the relative concentration variations

249   within our sample suite.

250

251   **3.2 Zn and Cu isotope analyses**

252

253   All isotopic analytical work was carried out in the MAGIC clean laboratories at

254   Imperial College London using deionized 18.2 MΩ water (MQ), Teflon-distilled acids

255   (HF, HNO_3 and HCl), Suprapur H_2O_2, and acid-cleaned Savillex PFA labware. 20 mg

256   of each sample was digested in a ~3:1 HF:HNO_3 mix at 140°C for ~48 hours. After

257   drying down to a gel-like consistency, samples were treated three times with

258   concentrated HNO_3 to drive off fluoride salts. Previously published high precision

259   trace element data for the same sample powders (Howarth et al., 2018) were used to

260   estimate the appropriate volume of a ^{64}Zn-^{67}Zn double spike required to obtain a Zn

261   spike:sample ratio of approximately 1.2 (Arnold et al., 2010; Bridgestock et al.,

262   2014). After spike equilibration, conversion to chloride, and re-dissolution in 7M HCl

263   + trace H_2O_2, Cu and Zn fractions were purified from the same digest solutions via

264   anion exchange using AG MP-1M resin (BioRad), as detailed previously (Maréchal et

265   al., 1999; Archer and Vance, 2004; Little et al., 2014b). Due to the highly refractory

266   nature of the samples (i.e. high concentrations of potentially interfering elements such

267 as Ti and Fe), three column passes were performed for both the Cu and Zn fractions.

268 The final Zn column was smaller in volume, following Bridgestock et al. (2014).

269

270 Prior to analysis, purified Cu fractions were refluxed overnight in $HNO_3 + H_2O_2$ and

271 purified Zn fractions were treated twice with ~100 μL HNO_3, with the intention of

272 eliminating residual resin-derived organics, before final re-dissolution in 1 mL 2%

273 HNO_3. Aliquots of these solutions were diluted to final concentrations of ~100ppb

274 total Zn (i.e. spike + sample Zn) and ~100ppb Cu for analysis. For both Cu and Zn,

275 the USGS rock standards BHVO-2, BIR-1A, BCR-2 and Nod-P1 were processed

276 using the same procedures and analysed to assess accuracy. Table 3 compares our

277 data with previously published $\delta^{66}Zn$ and $\delta^{65}Cu$ values.

278

279 Zinc isotope analyses followed protocols described previously (Arnold et al., 2010;

280 Bridgestock et al., 2014). Briefly, measurements were made on a Nu Plasma HR MC-

281 ICP-MS equipped with an ARIDUS II (CETAC Technologies) desolvating system

282 and nominal 100 μL/min MicroMist glass nebulizer, in low resolution mode.

283 Instrumental sensitivities were >100 V/ppm Zn. Data collection (3 × 20 5s

284 integrations) was preceded by an analysis (15 5s integrations) of the 2% HNO_3 used

285 to dilute solutions, with subtraction of these "on-peak zeroes" from sample signals.

286 Instrumental mass bias was corrected via the double spike technique described in

287 Arnold et al. (2010) and Bridgestock et al., (2014). Data reduction was carried out

288 offline following Siebert et al. (2001), with corrections for spectral interferences from

289 ^{64}Ni (via monitoring ^{62}Ni) and Ba^{2+} ions (via monitoring at mass 68.5). Interference

290 corrections were negligible, however, with $^{64}Ni^+/^{64}Zn^+$ and $^{134}Ba^{2+}/^{67}Zn^+$ levels at less

291 than 1×10^{-5} in all cases. The Zn isotope ratios of samples were determined relative

292 to matching (spike:natural Zn ratio and total Zn) standard solutions of IRMM-3702:

293 Eqn. 1: $\delta^{66}Zn = [(R_{Sample}/R_{Standard}) - 1] \times 1{,}000$

294 Final values are reported normalised to JMC Lyon by applying a correction of

295 +0.30‰, as recommended in the recent review by Moynier et al. (2017). Over the

296 course of this study the long-term reproducibility of a secondary standard, the in-

297 house 'London Zn', was $\delta^{66}Zn_{JMC-Lyon} = +0.08 \pm 0.07‰$ (n = 99, 2 SD), compared

298 with $+0.08 \pm 0.04‰$ (n = 10, 2 SD) reported by Arnold et al. (2010) and $+0.12 \pm$

299 0.04‰ (n = 6, 2 SD) by Larner and Rehkämper (2012). Total procedural blanks for

300   Zn were 3.6 ± 2.6 ng (n = 8, 1 SD), less than 1% of the Zn content of the smallest

301   sample. Yields were 104 ± 10% (1 SD).

302

303   Copper isotope analyses employed a Nu Plasma II HR MC-ICP-MS at Imperial

304   College London. Measurements were made in low resolution mode, with introduction

305   via a Peltier cooled (to 5°C) glass spray chamber coupled to a ~100 µL/min glass

306   nebulizer. Instrumental mass bias was corrected via doping with Ni following e.g.,

307   Ehrlich et al. (2004) and Larner et al., (2011). Nickel was chosen ahead of Zn for this

308   study because it has a first ionization potential (7.64 eV) close to that of Cu (7.72 eV)

309   and it is less sensitive to contamination. All samples and standards were doped to

310   achieve a Ni:Cu ratio of 3 to 4, matched to within ± 5%. Tests at variable Ni/Cu ratios

311   (2 to 5) suggested that neither accuracy nor precision is sensitive to the selected Ni:Cu

312   ratio. Analyses were carried out in static mode using Faraday cups to monitor masses

313   60, 61, 62 (for Ni), and 63, 65 (for Cu).

314

315   Data collection consisted of 60 x 5s integrations preceded by an analysis (15 x 5s

316   integrations) of the 2% HNO_3 solution, with the latter subtracted from sample signals.

317   Sensitivity for Cu was typically ~25 V/ppm. The exponential law was used to mass

318   bias correct measured $^{65}Cu/^{63}Cu$ ratios relative to $^{62}Ni/^{60}Ni$. $\delta^{65}Cu$ values were then

319   calculated as the deviation of the mass bias corrected $^{65}Cu/^{63}Cu$ ratio of the sample

320   relative to two bracketing standards (ERM-AE633):

321   Eqn. 2: $\delta^{65}Cu = [(R_{Sample}/R_{ERM\text{-}AE633}) - 1] \times 1{,}000$

322   This combination of external element doping and standard-sample bracketing has

323   previously been described for e.g., Tl with Pb (Nielsen et al., 2004) and for Cu with

324   Ni (Larner et al., 2011).

325

326   Finally, the minor reported offset of -0.01‰ between AE633 and the international

327   standard NIST SRM 976 was applied, such that data are reported normalised to SRM

328   976 (Moeller et al., 2012). The long-term reproducibility of a secondary Romil Cu

329   solution standard was $\delta^{65}Cu_{SRM\text{-}976}$ = +0.23 ± 0.07‰ (n = 22, 2 SD), comparable to

330   the +0.20 ± 0.08‰ (n = 5, 2 SD) reported by Larner et al. (2011). Total procedural

331   blanks for Cu were 4.9 ± 1.7 ng (n = 4, 1 SD), less than 1% of the Cu content of the

332   smallest sample. Yields, estimated by comparison of Cu concentration data from the

333 OU (Howarth et al., 2018) with concentrations from the isotopic analysis (obtained by

334 a less precise beam matching approach), were 93 ± 9% (1 SD). Complete yields are

335 essential for Cu isotope analyses due to the potential for isotopic fractionation during

336 anion exchange (Maréchal and Albarède, 2002); no relationship is observed between

337 sample isotopic composition and calculated yield, corroborating the accuracy of the

338 Cu isotope data presented here.

339

340 **3.3 Calculating CIA, IOL and τ –values**

341

342 Two useful measures of the degree of weathering are presented. First, the Chemical

343 Index of Alteration (CIA) is calculated following Nesbitt and Young (1982). CIA

344 utilises the molar mass of key indicator elements:

345 Eqn. 3: $CIA = [Al_2O_3/(Al_2O_3 + CaO^* + Na_2O + K_2O] \times 100$

346 [Where each compound is expressed as its molar mass]

347 CaO* is the amount of CaO incorporated in the silicate fraction of the rock. Since

348 CaO contents of the SQ samples are low (<1 wt%), and because inherent carbonate

349 phases were absent, no correction for the sample carbonate content was deemed

350 necessary. CIA effectively tracks feldspar dissolution and the concomitant release of

351 Ca, Na, and K relative to Al, since the latter is typically retained within resulting

352 clays. Most igneous rocks of varying composition will plot between a CIA value of 35

353 and 55, with mafic rocks occupying the lower values. Unaltered granites and

354 granodiorites, which may be representative of the greywacke protolith of the SQ

355 profile, have CIA values of between 45 and 55. By comparison, sample SQ2 has a

356 CIA value of 57 (Table 2; Fig. 2).

357

358 Second, Babechuk et al., (2014) suggest an alternative means to chemically

359 characterise the stages of extreme weathering at which the CIA becomes ineffective,

360 the Index of Lateritisation (IOL; Table 2, Fig. 2):

361 Eqn. 4: $IOL = 100 \times [(Al_2O_3 + Fe_2O_{3(T)}) / (SiO_2 + Al_2O_3 + Fe_2O_{3(T)})]$

362

363 Enrichment or depletion of an element can be quantified by comparison to an

364 immobile reference element. For this purpose, we calculate the tau (τ) parameter

365 (after Chadwick et al., 1990):

366 Eqn. 5: $\tau_{i/j} = \left[\dfrac{(\frac{C_i}{C_j})_h}{(\frac{C_i}{C_j})_p} \right] - 1$

367 Where C is the measured concentration, i is the element of interest (e.g.. Zn, Cu), j is

368 an immobile reference element (Nb, Ti or Zr), h is the weathering product, and p the

369 unaltered parent lithology. A value greater than zero indicates net gain of an element

370 relative to the parent material at that horizon within the weathering profile, while a

371 value less than zero indicates loss.

372

373 Two approaches were used to investigate uncertainty in τ –values. First, we compared

374 τ-values calculated assuming p is represented by the deepest sample in the section

375 (SQ2) with those calculated by taking an average of all samples from the little altered

376 zone I (SQ2 – SQ6). Second, Babechuk et al. (2014) advocate the use of Nb as the

377 most appropriate immobile reference element (j) for lateritic sample suites. In

378 addition, and for comparison, we compare τ-values calculated using Nb with those

379 determined using immobile elements Ti and Zr. Importantly, we find no significant

380 difference in absolute values or patterns of elemental enrichment or loss independent

381 of the choice of p or j (Fig. S2, Fig. 4).

382

383

384 **4.0 Results**

385

386 **4.1 Zn and Cu concentrations and enrichment-depletion patterns (τ-values)**

387

388 Copper concentrations exhibit limited absolute variability up-section (31 – 66 µg/g)

389 compared to larger variations in Zn (21 – 146 µg/g) (Table 2, Fig. 4A). Both Cu and

390 Zn concentrations decrease in stepwise fashion across the line of seepage, which

391 represents the transition from zone I to zone II at ~15m depth (Fig. 4A). Elevated

392 concentrations of both elements are observed at 7.5m (zone III, sample SQ11), the

393 uppermost depth of the paleo-water table (Wimpenny et al., 2007). The surface-most

394 sample (SQ14) has distinctly higher Cu and Zn concentrations compared to the other

395 two samples beneath; together these three samples make up the Fe-rich duricrust

396 (zone IV).

397   Both τ_{Zn} and τ_{Cu} become increasingly negative up section, with up to ~90% Zn and

398   ~70% Cu depletion relative to the protolith composition (Fig. 4B). The pattern of

399   enrichment and depletion of both elements above the line of seepage (at ~15m) is

400   similar, with marked depletion immediately above this transition, interrupted by a

401   sharp peak of enrichment at the paleo-water table, followed by more moderate

402   enrichment in the uppermost sampling horizon (SQ14, particularly evident for τ_{Cu}).

403   τ_{Zn} exhibits a very strong correlation with τ_{Li} throughout the laterite profile, while τ_{Cu}

404   is decoupled from both τ_{Li} and τ_{Zn} in zone I, at 15m and below (Fig. 4B).

405

406   **4.2 Zn and Cu isotope systematics**

407

408   The unaltered greywacke protolith, represented by sample SQ2 at 34 m, has a Zn

409   isotope composition of +0.50 ± 0.04‰ (n = 2, 2SD). This value is isotopically heavy

410   compared to typical lithogenic Zn in clastic sediments, at +0.28 ± 0.13‰ (n = 105,

411   Moynier et al., 2017). For Cu, sample SQ2 has a Cu isotope value of +0.03 ± 0.05‰

412   (n = 2, 2SD), which is within the typical range for Cu in clastic sediments at +0.08 ±

413   0.20‰ (n = 42, Moynier et al., 2017).

414

415   In the low alteration zone I, below the line of seepage (samples SQ2 to SQ6, 34 to 15

416   m), Zn isotope ratios do not vary outside of analytical uncertainty ($\delta^{66}Zn$ = +0.47 ±

417   0.09‰, n = 5, 2SD). Copper isotope ratios show a resolvable shift from ~0‰ at the

418   base of the profile to lower values at 22.5m (SQ5, -0.28‰) and 15m (SQ6, -0.23‰)

419   (Fig. 5A).

420

421   Above the line of seepage in zones II–IV (15 m – surface), samples SQ7 to SQ14

422   show considerably more marked, correlated shifts in Zn and Cu isotope compositions.

423   This is manifest as a general trend towards lower $\delta^{66}Zn$ and $\delta^{65}Cu$ upwards in the

424   weathering profile (Fig. 5). Again, the paleo-water table interrupts this trend in $\delta^{65}Cu$,

425   with a marked offset towards a higher Cu isotope ratio (at -0.30‰) compared to the

426   samples directly above and below (at -0.86‰ and -0.65‰ respectively). The surface-

427   most sample (SQ14) is isotopically lightest for both Cu (at -0.87‰) and Zn (at -

428   0.02‰). In summary, the total variability up section in $\delta^{65}Cu$ is 0.91‰, which is

429   greater than that observed for $\delta^{66}Zn$, at 0.55‰.

430

431

5.0 Discussion

433

5.1 Zone I: Host phases and lithological heterogeneity in the low alteration zone (parent – saprock)

436

437 Wimpenny et al. (2007) described the mineralogical variations through the SQ
438 sequence, which we briefly recount here. The deepest greywacke sample (SQ2, 34 m)
439 comprises 75% quartz, 15% biotite, 5% plagioclase, 2% opaques and 3% other
440 minerals (Wimpenny et al., 2007). Up-section in zone I (SQ2 – SQ6 at 34 – 15m),
441 lithological variability is observed (Fig. 3). For example, biotite contents vary
442 between 8 and 20%, plagioclase from 2 – 8% and quartz from 74 – 80%. Secondary
443 clay minerals (e.g., kaolinite) are not observed in zone I (Fig. 3), confirming the
444 limited extent of chemical weathering at these depths. CIA values are consistent with
445 this inference, and remain essentially unchanged between the base of the profile (CIA
446 = 57 at 34m) to the top of zone I (CIA = 59 at 15m; Fig. 2)

447

448 Lithological variability is reflected in the major and trace element geochemistry of the
449 zone I samples. Al_2O_3, Fe_2O_3, MgO, Li and many other trace element concentrations
450 positively co-vary with biotite crystal content in this zone (Table S1, S3; Fig. S3).
451 SiO_2 concentrations show the opposite trend (Fig. S4). These observations are
452 consistent with known minor lateral variation in the quarry (Hibbert, 2017) and are
453 likely linked to a grain size control on mineralogy and geochemistry, as previously
454 recognised in sedimentary settings (e.g., Vdović et al., 1991; Roser et al., 1996;
455 Lupker et al., 2011). Accordingly, Al_2O_3 and SiO_2 contents generally correlate and
456 anti-correlate with grain size respectively, due to the predominance of aluminium-rich
457 phyllosilicates (like biotite) in the fine grain size fraction.

458

459 Zinc concentrations in zone I samples correlate with biotite content (Fig. S3B), as
460 well as with several trace elements and major oxides that are commonly hosted in
461 biotite, including Li, Co, Rb, Cs and Tl, MnO, MgO and K_2O (Fig. 6A, C, data from
462 Howarth et al., 2018). Potassium and Mg are both key structural components in

463   biotite ($K_2(Mg,Fe^{2+})_{6-4}(Fe^{3+},Al,Ti)_{0-2}[Si_{6-5}Al_{2-3}O_{20}](OH,F)_4$) (Deer et al., 1992).

464   Manganese and Li are commonly substituted into biotite octahedral sites, and Cs, Rb

465   and Tl commonly replace K in interlayer sites (Deer et al., 1992; Gomez-Gonzalez et

466   al., 2015). These observations suggest that the Zn present in the parent greywacke is

467   principally hosted within biotite.

468

469   Both Zn and Cu are chalcophile and, if sulphide phases were present, would be

470   expected to strongly partition into these phases. However, measured S concentrations

471   in the SQ profile are low (<0.1 wt%, Fig. 6, Table 2) and, while there is a positive

472   correlation between Zn and S concentrations in zone I samples (Fig. 6G), a negative

473   correlation is observed between Cu and S concentrations (Fig. 6H). This observation

474   appears to rule out the presence of CuS phases in the parent lithology. Furthermore,

475   Banks (1973) reports $116 - 316$ µg/g S in biotite, suggesting that biotite-hosted S

476   provides a satisfactory explanation for the correlation of Zn with S (Fig. 6G).

477

478   In contrast to Zn, Cu shows negative correlations with almost all elements in zone I

479   except SiO_2 and Na_2O (Fig. 6). As discussed, higher SiO_2/Al_2O_3 ratios likely reflect a

480   coarser grain size. Higher Na_2O contents in sandstone versus siltstone have been

481   hypothesised to reflect a greater abundance of detrital plagioclase (Roser et al., 1996),

482   but no correlation is observed between Na_2O and plagioclase abundance in the SQ

483   sample set. Plagioclase contains only scarce quantities of trace elements (Deer et al.,

484   1992), in any case, making this an unlikely Cu host. We conclude that identification

485   of the Cu host phase(s) requires detailed micro-analytical work that is beyond the

486   scope of this study. Nevertheless, we suggest that Cu is present in one or more detrital

487   phase(s), the abundance of which is greater in the coarser grained beds of the

488   greywacke.

489

490   To summarise, the τ_{Zn} and τ_{Cu} values in zone I samples similarly reflect primary

491   lithological heterogeneity of the greywacke, rather than recording any elemental mass

492   transfer. Thus, in order to take account of this heterogeneity in calculating τ-values,

493   we use an average of all samples in zone I as the best estimate of the parent material

494   ('p' in Eqn. 5). This approach, rather than simply selecting the least altered sample

495   SQ2, leads to a greater coherence of the calculated τ-profiles for different elements

496   (e.g., Zn cf. Li) and for the same element using different immobile reference elements

497   (e.g., Ti, Zr, 'j' in Eqn. 5; Fig. S2).

498

499   Isotopically, the greywacke δ^{65}Cu lies within the range of typical clastic sediments, at

500   about 0‰ (Moynier et al., 2017). For δ^{66}Zn, however, it is isotopically heavy (e.g.,

501   sample SQ2 at +0.50‰) relative to lithogenic Zn (at about +0.3‰; Moynier et al.,

502   2017). Similarly isotopically heavy Zn has been observed in biotite-granites from the

503   Kaapvaal craton, South Africa (Doucet et al., 2018), from Taiwanese andesite,

504   sandstones and suspended river sediment (Bentahila et al., 2008), and in granitoids

505   from the Nyong Basin, Cameroon (Viers et al., 2007) and the Lachlan Fold Belt,

506   Australia and Black Hills, South Dakota, USA (Telus et al., 2012).

507

508   At 22.5m (sample SQ5), a small shift (of about –0.3‰) towards a lower δ^{65}Cu value

509   is observed (Fig. 5). This shift may either be a primary lithological signature, or

510   indicate the earliest detectable onset of oxic chemical weathering. Sample SQ5 has

511   the highest phyllosilicate abundance (sum of biotite, muscovite and chlorite, 23%;

512   Table S1, Fig. 3) and a slightly elevated CIA value (of 63; Table 2, Fig. 2) compared

513   to the other samples in zone I (at 12–15% and 57–59 respectively). The high

514   abundance of easily weatherable, fine fraction phyllosilicates increases the

515   susceptibility of this sample to alteration (Goldich, 1938).

516

517   Overall, elemental variations in the low alteration zone I can primarily be explained

518   by lithological heterogeneity in the parent greywacke. Copper and Zn isotopes in this

519   zone exhibit small shifts, either reflecting this lithological heterogeneity and/or early

520   stage chemical alteration. A greater spatial resolution of sampling in the quarry would

521   improve constraints on the importance of lateral variability and lithological

522   heterogeneity.

523

524

525   **5.2 Zones II and IV: the Mottled and Laterite Zones**

526

527   Above the line of seepage, the mottled and laterite zones (II and IV) are characterised

528   by depletion of Cu and Zn (observed in negative τ_{Cu} and τ_{Zn}) and isotopically light

529   δ^{65}Cu and δ^{66}Zn values (Figs. 4, 5). This pattern could reflect either (i) preferential

530 release of heavy isotopes during mobilization from (i.e. dissolution of) the host phase,

531 or (ii) isotope fractionation in the aqueous phase and/or during precipitation of

532 secondary Fe oxide phases.

533

534 *5.2.1 Isotope fractionation during host mineral dissolution*

535

536 Mineral dissolution may be accompanied by isotope fractionation. For example,

537 isotopically light Zn and Cu in weathered black shales from China and the USA have

538 been interpreted to result from preferential release of heavy Cu and Zn isotopes

539 during oxidative weathering of sulphide minerals (Mathur et al., 2005; Fernandez and

540 Borrok, 2009; Kimball et al., 2009; Mathur et al., 2012; Lv et al., 2016). However, the

541 greywacke lithology of the SQ laterite is sulphide-poor, and neither Cu nor Zn

542 appears to be dominantly hosted in a sulphide phase (Section 5.1).

543

544 The alternation of wet and dry seasons results in oscillating reducing and oxic

545 conditions in the developing weathering profile. Under water-saturated conditions, Fe

546 (as ferrous Fe^{2+}) is mobile, while during drier periods this Fe precipitates as ferric Fe

547 oxides, forming the Fe-rich mottles of zone II. Hence, redox changes play an

548 important role in mineral breakdown, the removal of mobile elements, and the

549 formation of secondary minerals enriched in Fe_2O_3 and Al_2O_3. Zinc is not redox

550 active, but mobilization of Cu via Cu(II) reduction has been hypothesised for

551 waterlogged soils and wetland systems (Bigalke et al., 2010c; Bigalke et al., 2013;

552 Babcsányi et al., 2014). However, Cu(II) to Cu(I) reduction is associated with release

553 of the light isotope of Cu (Bigalke et al., 2010c; Bigalke et al., 2013; Babcsányi et al.,

554 2014). The preferential release of light Cu isotopes from host mineral phases via

555 Cu(II) reduction is inconsistent with the isotopically light solid residue observed in

556 the SQ laterite. Hence, though oscillating redox is an important process in

557 lateritization, alone it cannot explain the observed Zn and Cu isotope variations.

558

559 In abiotic, proton-promoted dissolution experiments investigating the release of Fe

560 from hornblende, a small light isotope fractionation is observed (Brantley et al.,

561 2001). Similar light isotope fractionation of Fe and Zn is observed during dissolution

562 of granite with HCl (Chapman et al., 2009; Weiss et al., 2014). This preferential

563 release of light isotopes during proton-promoted dissolution likely reflects a kinetic

564 isotope fractionation. Again, preferential mobilization of light isotopes is inconsistent

565 with the isotopically light residue observed in the SQ weathering profile.

566

567 In natural aqueous solutions both Zn and Cu are dominantly complexed to strong

568 organic ligands (McBride, 1981; Coale and Bruland, 1988; e.g., Bruland, 1989; Xue

569 et al., 1995; Moffett and Brand, 1996; Wells et al., 1998; Shank et al., 2004; Grybos

570 et al., 2007; Hoffmann et al., 2007; Vance et al., 2008). It is well documented that

571 mineral dissolution rates are enhanced above proton-promoted rates by the presence

572 of organic ligands, via a ligand-promoted dissolution mechanism (e.g., Berthelin and

573 Munier-Lamy, 1983; Amrhein and Suarez, 1988; Bennett, 1991; Welch and Ullman,

574 1993; 1996; 2000). For example, release of Cu from Columbia River Basalt was

575 elevated in a batch experiment containing an organic ligand (citrate) compared to the

576 inorganic control (Neaman et al., 2005b). At equilibrium, organic complexation is

577 associated with preferential chelation of heavy isotopes (Dideriksen et al., 2008;

578 Jouvin et al., 2009; Bigalke et al., 2010b; Morgan et al., 2010; Fujii and Albarede,

579 2012; Fujii et al., 2013; Sherman, 2013; Fujii et al., 2014; Ryan et al., 2014; Marković

580 et al., 2017). Therefore, at equilibrium, ligand-mediated dissolution should be

581 associated with release of isotopically heavy Zn and Cu, consistent with the observed

582 isotopically light laterite residue.

583

584 We model this scenario as a simple open-system Rayleigh distillation process in

585 Figure 7. In this model, we envisage that the isotopically heavy, organically

586 complexed pool is continuously removed from the profile under a constant

587 fractionation factor. For Zn, the Rayleigh model isotope fractionation factor that best

588 fits the data is of the order $\alpha = 1.0002$, i.e. $\Delta^{66}Zn_{aqueous-solid} \approx +0.2‰$ (Fig. 7A). For

589 Cu, the required fractionation factor is larger, at about $\alpha = 1.001$ or $\Delta^{65}Cu_{aqueous-solid} \approx$

590 +1.0‰ (Fig. 7B). The fractionation factors derived from the Rayleigh approach can

591 only be confidently ascribed meaning for a single-step process, e.g., mobilization

592 from the host mineral phase. Several processes are operating and, likely, fractionating

593 Zn and Cu isotopes during lateritization. Nevertheless, the Rayleigh model produces

594 an acceptable fit to the data in spite of its simplicity (Fig. 7), and we proceed to

595 compare our model-derived fractionation factors to those for organic complexation of

596 Zn and Cu in the literature.

597

The magnitude of Zn and Cu isotope fractionation on organic complexation is a

function of the stability constant of complex formation (Ryan et al., 2014; Marković

et al., 2017). Organic ligands in freshwater solutions fall into two categories: low

molecular weight organic acids (or 'L1-type' ligands, e.g., polyphenols, hydroxamate

siderophores), and soluble humic/fulvic acids (Harter and Naidu, 1995). While

humic/fulvic acids generally have relatively weak stability constants (at around $\sim 10^7 -$

10^9), L1-type ligands can be much stronger (up to $\sim 10^{25}$). Copper has a particular

affinity for strong organic ligands (as compared to, e.g., Zn and Cd; Benedetti et al.,

1995; Xue et al., 1995; McBride et al., 1997). Relatedly, the magnitude of isotope

fractionation for organic complexation is also larger for Cu compared to Zn

(Marković et al., 2017; cf. Ryan et al., 2014).

609

A fractionation factor $\Delta^{66}Zn_{\text{aqueous-solid}} \approx +0.2$‰ (Fig. 7A) is consistent with an

experimental estimate of isotope fractionation for Zn complexation with purified

humic acid ($\Delta^{66}Zn_{\text{humic-aquo}} = +0.24 \pm 0.06$‰; Jouvin et al., 2009). By comparison, the

larger fractionation factor for Cu ($\Delta^{65}Cu_{\text{aqueous-solid}} \approx +1.0$‰; Fig. 7B) implies

complexation by complexes stronger than humic acids, which have a reported range

in $\Delta^{65}Cu_{\text{humic-aquo}}$ of +0.24 to + 0.55‰ (Bigalke et al., 2010b; Sherman, 2013; Ryan et

al., 2014). Sherman (2013) predicts a fractionation factor for a L1 ligand model

complex (Cu acetohydroxamate) of $\Delta^{65}Cu_{\text{hydroxamate-aquo}} = +1.1$‰, while Ryan et al.

(2014) measured fractionation factors of up to +0.84‰ for strong synthetic L1-type

ligands. Both of these estimates would be consistent with the Rayleigh model

prediction.

621

In practice, it is unclear if chemical equilibrium between the rock and aqueous phase

(or something approaching it) can be obtained during weathering. Contrary to the

predicted release of heavy isotopes during ligand-promoted dissolution, dissolution of

granite in the laboratory in the presence of oxalic acid resulted in release of

isotopically *light* Zn (Weiss et al., 2014). Similarly, Brantley et al. (2004) and

Wiederhold et al. (2006) observed release of isotopically light Fe in ligand-mediated

leaching experiments with hornblende and goethite, respectively. However, these

leaching experiments were not at equilibrium, and the observed light isotope

fractionation may reflect a kinetic control. By contrast, long duration experiments of

631   Wiederhold et al. (2006) did exhibit the predicted reverse trend, with isotopically

632   heavy Fe in solution. It remains to be determined whether these longer duration

633   experiments more closely reflect processes operating in more advanced (i.e., lateritic)

634   weathering environments.

635

636   Mineral dissolution rates in the lab are typically one to three orders of magnitude

637   faster than in the field (e.g., Swoboda-Colberg and Drever, 1993; Kump et al., 2000;

638   Brantley, 2003). In the lab, dissolution rates are thought to be interface-limited, i.e.

639   the rate of reaction is determined by the dissolution rate of the mineral (Brantley,

640   2003). By contrast, mineral dissolution rates in a transport-limited scenario are

641   controlled by the rate of diffusion or advection in solution (Brantley, 2003). Mineral

642   dissolution is likely predominantly interface-limited in the field (see discussion in

643   Kump et al., 2000), but it can be transport-limited at low water-rock flushing rates

644   (Schnoor, 1990; Kump et al., 2000). This difference may partially explain the offset in

645   lab and field-derived mineral dissolution rates, with transport-limited dissolution

646   operating more slowly than interface-limited dissolution (Kump et al., 2000).

647

648   Lateritic weathering is likely to occur in a transport-limited (also called "supply

649   limited"; West et al., 2005) weathering regime, with low denudation rates coupled to

650   high weathering intensity (White and Buss, 2014). Weathering fluxes in this scenario

651   reflect thermodynamic constraints, with chemical weathering reactions occurring

652   close to equilibrium (White and Buss, 2014). Indeed, this regime is sometimes

653   referred to as 'local-equilibrium' (Lebedeva et al., 2010; Brantley and Lebedeva,

654   2011). Hence, we suggest that transport-limited mineral dissolution may be associated

655   with equilibrium isotope fractionation, while interface-limited mineral dissolution will

656   typically be kinetically controlled (e.g., Brantley et al., 2004; Wiederhold et al., 2006;

657   Weiss et al., 2014). If this hypothesis were correct, ligand-mediated mineral

658   dissolution at equilibrium would promote release of heavy Zn and Cu isotopes,

659   consistent with observations in the SQ laterite (see also section 5.2.2). The corollary

660   of this hypothesis, however, would predict kinetic isotope fractionation (i.e.

661   mobilization of light isotopes) in kinetic-limited (or 'weathering-limited') regimes, in

662   which the physical removal of eroded material is faster than its breakdown by

663   chemical weathering. There is limited evidence for this prediction in Zn and Cu

664   isotope weathering studies to date. We return to this topic in section 5.4.1.

665

666   To summarise, the isotopically light compositions observed in the SQ laterite residue

667   may reflect ligand-mediated dissolution of their host phases, if dissolution is

668   occurring close to equilibrium in a transport-limited regime. By contrast, mobilization

669   via either a kinetic or reductive (in the case of Cu) mechanism would be associated

670   with preferential release of isotopically light Zn and Cu. In this case, the salient

671   isotope fractionation during lateritic weathering must occur after Zn and Cu

672   mobilization, in pore waters and/or during precipitation of secondary minerals.

673

674   *5.2.2 Isotope fractionation in the aqueous phase*

675

676   As discussed, Zn and Cu will be dominantly complexed by organic ligands in the

677   aqueous phase (e.g., McBride, 1981; Xue et al., 1995; Grybos et al., 2007; Hoffmann

678   et al., 2007), and organic complexation is associated with chelation of heavy Zn and

679   Cu isotopes (Jouvin et al., 2009; Bigalke et al., 2010b; Fujii and Albarede, 2012; Fujii

680   et al., 2013; Sherman, 2013; Fujii et al., 2014; Ryan et al., 2014; Marković et al.,

681   2017). By comparison, the free or weakly complexed pool of Zn or Cu will be

682   isotopically light. Taking Cu as an example, free Cu^{2+} and organically complexed Cu

683   and are isotopically offset by up to −1.1‰ (Sherman, 2013). In a closed system at

684   isotopic equilibrium, the Cu isotope composition of organically complexed Cu (δ_{org})

685   is constrained by this fractionation factor ($\Delta_{free\text{-}org}$) and the ratio of organically

686   complexed Cu to free Cu (N_{org}/N_{free}), as described by equation 6 (modified after

687   Stevenson et al., 2017):

688   Eqn 6: $\delta_{org} = \delta_{system} - \dfrac{\Delta_{free\text{-}org}}{1+\frac{N_{org}}{N_{free}}}$

689   In nature, N_{org}/N_{free} for Cu is always very high – i.e. Cu is almost quantitatively

690   organically complexed. Thus, mass balance constraints dictate that organically

691   complexed Cu in solution will closely reflect the isotopic composition of the Cu that

692   is mobilized during weathering, while the free Cu species will be fractionated by as

693   much as −1.1‰. Consequently, in a scenario in which Zn and Cu are organically

694   complexed in pore waters, secondary mineral phases may simply scavenge the

695   isotopically light uncomplexed (or weakly-complexed) pool of Zn and Cu (as

696   proposed by Vance et al., 2016).

697

5.2.3 Isotope fractionation during coprecipitation with aluminous Fe oxide

An alternative mechanism to explain the light isotopic composition of the laterite residue is light Zn and Cu isotope fractionation associated with precipitating Fe oxide phases. For example, Viers et al. (2007) observed isotopically light Zn in laterite samples from Cameroon, which they attributed to 'ferrugination', a term which implies preferential incorporation or sorption of light isotopes in or on precipitating Fe oxide phases. Suhr et al. (2018) suggested a similar process to explain isotopically light Zn in the residue of a basaltic laterite from Bidar, India. We observe negative correlations of $\delta^{66}Zn$ and $\delta^{65}Cu$ with Fe_2O_3 (Fig. 8), indicating that Fe oxide formation may well play a role in the very light isotopic compositions of Cu and Zn in zone II and IV samples.

Can ferrugination alone lead to isotopically light Zn and Cu in the laterite residue? Most experimental studies have focussed upon inorganic *sorption* of Zn and Cu on Fe oxide (or other mineral) surfaces, with the prevailing paradigm that such sorption is typically associated with preferential accumulation of heavy isotopes on the mineral surface (Pokrovsky et al., 2005; Balistrieri et al., 2008; Juillot et al., 2008; Pokrovsky et al., 2008; Bryan et al., 2015; Guinoiseau et al., 2016). Preferential sorption of heavy isotopes on precipitating oxide surfaces would be contrary to the observed light isotopic compositions of laterite samples in zones II and IV.

The dominant Fe oxide phases present in the SQ samples are aluminous goethite and aluminous haematite (Table S1; Wimpenny et al., 2007). Both phases can also *incorporate* Zn^{2+} and Cu^{2+} into their structures, via substitution for Fe^{3+} on octahedral (VI-fold coordinated) sites (e.g., Cornell and Giovanoli, 1988; Gerth, 1990; Manceau et al., 2000; Cornell and Schwertmann, 2003). Incorporation of significant Zn (19.9 µg/g) and Cu (31 µg/g) in goethite and haematite, comparable to the concentrations observed in the indurated SQ duricrust (Zn: 25 – 31 µg/g, Cu: 39 – 61 µg/g), has been suggested for lateritic samples from Western Australia (Anand and Gilkes, 1987; Singh and Gilkes, 1992). Preferential incorporation of isotopically light Zn and Cu into precipitating aluminous Fe oxides could thus provide a mechanism to drive the laterite residue isotopically light.

732   The trajectory of the dashed arrow in Figure 9A implies a maximum effective isotopic

733   fractionation factor on incorporation of Zn into Fe oxides of $\Delta^{66}Zn_{Fe\ oxide-aqueous} \approx -$

734   0.7‰ (Fig 9A). A conference abstract indicates that Zn incorporation in goethite may

735   indeed be associated with a preference for the light Zn isotope, though the magnitude

736   of associated isotope fractionation is not reported (Becker et al., 2014). In the case of

737   Cu, the equivalent maximum effective isotope fractionation factor described by the

738   trajectory of the dashed arrow in Figure 9B is about –1.3‰. Experiments measuring

739   isotope fractionation on incorporation of trace metals in Fe (and other, e.g., Al) oxides

740   are an important avenue for future research.

741

742   To conclude, we postulate that a combination of strong complexation by organic

743   ligands in association with the retention of light isotopes in or on secondary

744   aluminous Fe oxide phases can explain the residual light Zn and Cu isotope signatures

745   of the zone II and IV laterite samples. If ferrugination alone is driving the light

746   isotopic composition of the laterite residue, Zn and Cu must be incorporated in (rather

747   than sorbed on) Fe oxide phases. Micro-analytical techniques, such as EXAFS, may

748   allow identification of the phase association and crystal chemistry of Zn and Cu in

749   laterite samples.

750

751   *5.2.4 Upper horizon: a role for organic matter?*

752

753   Surface organic-rich layers of soils are often enriched in light Zn and Cu isotopes,

754   which has been related to the uptake and recycling of plants (e.g., Bigalke et al., 2011,

755   2010a; Liu et al., 2014; Vance et al., 2016; Weiss et al., 2007). Therefore, the

756   presence of isotopically light solid organic matter in the uppermost sample of the SQ

757   weathering profile is plausible, given that the surface of the lateritic mesa into which

758   the quarry has been excavated is characterized by well-developed sub-tropical scrub

759   vegetation, predominantly acacia. The uppermost sample (SQ14) is slightly enriched

760   in Cu and Zn relative to the other two indurated laterite duricrust samples (SQ12 and

761   SQ13), and is indeed the isotopically lightest sample in the whole section ($\delta^{66}Zn = -$

762   0.02‰ and $\delta^{65}Cu = -0.89$‰; Figs. 3 and 4). Unfortunately, we lack sufficient

763   sampling resolution to evaluate in detail the role of recent biological activity and

764   modern soil formation in the uppermost meters of the weathering profile.

765

5.3 Zone III: the Paleo-water Table

Previous studies have noted considerable major and trace element and isotope variability associated with the paleo-water table zone III (at 7 – 8.5 m depth, samples SQ10 and SQ11; Howarth et al., 2018; Wimpenny et al., 2007; Widdowson, 2009), which represents a transition from sub-oxic to fully oxidising conditions (Wimpenny et al., 2007). There are two ways of interpreting this zone of alteration. To date, it has been suggested to be at the top of a 'classic' groundwater level that was abandoned during uplift (Wimpenny et al., 2007). As such, it is considered to have developed through a combination of open system, allochthonous input of trace elements from circulating groundwaters, and the precipitation of Fe and Mn-oxides, which act as effective scavengers of other elements (Howarth et al., 2018; Wimpenny et al., 2007; Widdowson, 2009).

An alternative interpretation suggests that zone III was at the base of an ancient, episodic stagnant water body (i.e. seasonally present between the surface and ~8 m depth). In this case, water would have accumulated at a depth with reduced water permeability at the base of zone III during the rainy season, and zones III and IV could be considered together as a single lateritized package that subsequently underwent uplift, drying and hardening to form the present duricrust. In this scenario, the Fe-rich mottles in zone II (i.e. at depths below ~8 m) would reflect a second phase of waterlogging and lateritization, with seasonal stagnant water pooling close to the present day line of seepage (at ~15 m depth). This idea, of two repeating packages of lateritic alteration, could plausibly explain the τ_{Zn}, τ_{Cu} and Zn and Cu isotope data (Figs. 4B, 5A). However, we would expect to observe Fe enrichment at the line of seepage, equivalent to that observed in zone III (Fig. 4C), and no such Fe (or Mn) enrichment is observed. Further sampling at higher resolution, and laterally within the quarry, would help reconcile these two scenarios. For the purpose of this study, we consider that the distinct geochemistry of the samples in zone III deserve separate treatment to the more predictable upwardly progressing alteration characteristics of the remainder of the profile.

Evidence for the allochthonous input of elements to zone III is demonstrated through the behaviour of τ_{Fe} and τ_{Mn} values (Fig. 4C, Table 2). Both τ_{Fe} (18.9) and τ_{Mn} (5.5)

800   show extreme enrichment at 7.5m (SQ11), while τ_{Fe} (4.6) is also considerably

801   enriched at 8.5m (SQ10). The allochthonous input of elements to the profile can be

802   quantified by calculating integrated τ-values, weighting taus for each horizon (h) by

803   density (ρ) and thickness (z), following Vance et al. (2016):

804   Eqn. 6: $\tau_i^{int} = \dfrac{\sum_{h=0}^{n}(\tau_h \rho_h z_h)}{\sum_{h=0}^{n}(\rho_h z_h)}$

805   where i refers to the element of interest (Zn or Cu). This approach assumes negligible

806   denudation (physical erosion) of the weathering profile during development.

807

808   Positive integrated τ_{Fe}^{int} (1.5) and, marginally, τ_{Mn}^{int} (0.02) values (Table 2), suggest that

809   the zone III enrichments in τ_{Fe} and τ_{Mn} cannot simply be explained by redistribution

810   of these elements vertically (from zone II or IV, depending on the location of the

811   water body) in the weathering profile. If we assume allochthonous input of Fe and Mn

812   at the paleo-water table depths and exclude these zone III samples from the integrated

813   τ calculations (giving $\tau_i^{int-III}$ values), we find a negative integrated $\tau_{Mn}^{int-III}$ (–0.21) value,

814   consistent with that calculated for $\tau_{Li}^{int-III}$ (–0.21) and $\tau_{Zn}^{int-III}$ (–0.22). $\tau_{Fe}^{int-III}$ remains

815   positive, however, at 0.36, suggesting 30 to 40% Fe addition to the weathering profile

816   during alteration.

817

818   Both Cu (52 µg/g) and Zn (97 µg/g) show enrichment in zone III, with τ_{Cu} = 0.8 and

819   τ_{Zn} = 0.5 at 7.5m (SQ11, Fig. 4B). Integrated τ_{Zn}^{int} and τ_{Cu}^{int} values are negative,

820   however, both including (τ_{Zn}^{int} = –0.23, τ_{Cu}^{int} = –0.07) and excluding ($\tau_{Zn}^{int-III}$ = –0.22,

821    $\tau_{Cu}^{int-III}$ = –0.06) the zone III samples (Table 2). Therefore, the enrichments of Zn and

822   Cu in zone III do not *require* an allochthonous source of these two elements, though

823   such a source is not excluded.

824

825   The enrichments in Cu and Zn in zone III are restricted to a narrow depth range,

826   sampled at SQ11 only (7.5m, Fig. 4B). This pattern is similar to the narrow band of

827   enrichment observed for Mn (Fig. 4C) and contrasts with that of Fe, which is

828   significantly elevated across both SQ10 and SQ11 (8.5 – 7.5m; Fig. 4C). Manganese

829   oxide develops large areas of negative charge under the pH conditions of natural

830   waters, as a consequence of its low pH point of zero charge and relatively high

831   specific surface area (Catts and Langmuir, 1986). These characteristics make it a very

832   effective sorbent for other trace metals (e.g., Aplin and Cronan, 1985; Balistrieri and

833   Murray, 1986; Koschinsky and Hein, 2003; Peacock and Sherman, 2007; Tessier et

834   al., 1996). Accordingly, we suggest that Cu and Zn are scavenged by a precipitating

835   Mn oxide phase at the paleo-water table, rather than by the abundant Fe oxide phases

836   (as suggested for the zone II and IV samples; section 5.2). Sequential leaching

837   experiments would be required to further test this hypothesis.

838

839   Sample SQ11 is marked by an excursion towards isotopically heavier Cu compared to

840   the samples below and above, indicating scavenging of heavy Cu (Figs. 5, 7). In the

841   case of Zn, there is no resolvable shift in δ^{66}Zn (at +0.14‰) compared to the samples

842   above and below. In both cases sample SQ11 is distinct from the coherent $\tau-\delta$ trends

843   observed throughout the rest of the profile, which are reasonably well described by a

844   simple Rayleigh model (as described in Section 5.2.1; Fig. 7). There are two possible

845   explanations for the enrichment and distinct isotopic composition of SQ11: first, a

846   source with an isotopically heavy Cu isotope composition, or second, a source

847   combined with *in situ* isotope fractionation on sorption to the postulated Mn-oxide

848   phase.

849

850   Aerosols are one possible external source of trace metals to weathering profiles, and

851   are typically approximately lithogenic in Zn and Cu isotope composition (δ^{66}Zn

852   ~0.3‰ and δ^{65}Cu ~0‰; Dong et al., 2013; Little et al., 2014b). Based on the data in

853   this study, a locally derived lateritic aerosol source would be very isotopically light,

854   however, inconsistent with the shift toward heavier Cu isotope compositions at the

855   depth of the paleo-water table. Further, assuming an atmospheric route for aerosol

856   deposition, any aerosol addition should also be apparent as enrichment at the surface-

857   most depths of the laterite profile; such behaviour is not observed for the SQ profile.

858

859   Solute-laden groundwater has previously been suggested as providing an external

860   source of Re, Os, and Tl, to the SQ laterite, possible due to its low-lying topographic

861   position (Howarth et al., 2018; Wimpenny et al., 2007). Relatively few constraints

862   exist on the isotopic composition of Zn and Cu in groundwater, however. An

863   isotopically heavy groundwater source of Cu is certainly plausible, given observations

864   of isotopically heavy Cu in the dissolved phase in rivers (+0.02 to +1.45‰, discharge-

865   weighted average of +0.68‰; Vance et al., 2008). A groundwater-borne source of Zn

866   at about +0.2‰ is also possible, given the range of dissolved $\delta^{66}Zn$ in global rivers (−

867   0.12 to +0.88‰, discharge-weighted average of +0.33‰; Little et al., 2014b) and

868   mountain streams (+0.02 to +0.46‰, Borrok et al., 2008). Future isotope studies

869   should target groundwater in conjunction with surface-flowing water bodies.

870

871   Isotope fractionation may occur on sorption to the postulated Mn oxide phase. Bryan

872   et al. (2015) investigated Zn isotope fractionation on inorganic sorption to synthetic

873   birnessite (δ-MnO_2), a phyllomanganate phase common in terrestrial environments

874   (e.g., Taylor et al., 1964; Ross et al., 1976; Tokashiki et al., 1986; Uzochukwu and

875   Dixon, 1986; Post, 1999). At low ionic strength (applicable to freshwater

876   environments) they observe negligible Zn isotope fractionation, which is attributed to

877   the formation of octahedral surface complexes (Manceau et al., 2002); i.e. there is no

878   marked change in coordination environment on sorption compared to the hydrated

879    $Zn(H_2O)_6^{2+}$ ion present in solution (Bryan et al., 2015). Sorption of ~V-fold

880   coordinated hydrated Cu^{2+} on δ-MnO_2 is predicted to be associated with an

881   enrichment in heavy isotopes, due to the formation of tetrahedral surface complexes

882   (Manceau et al., 2002; Sherman and Peacock, 2010; Little et al., 2014a), though an

883   experimental study observed the opposite: preferential sorption of light Cu isotopes

884   on δ-MnO_2 ($\Delta^{65}Cu_{MnO2\text{-}aqueous}$ = −0.45 ± 0.18‰, n=12; Ijichi et al., 2018).

885

886   As described, the paleo-water table sample SQ11 is unusual in that it is unfractionated

887   in $\delta^{66}Zn$ and isotopically heavy in $\delta^{65}Cu$ compared to the samples above and below,

888   thus partly consistent with these inorganic predictions for sorption of hydrated Zn^{2+}

889   and Cu^{2+} on δ-MnO_2. However, the system is underconstrained: we lack information

890   about the isotopic composition of the contemporaneous fluid. Speciation in the natural

891   environment is more complex compared to these inorganic experimental and

892   theoretical considerations. In future, more realistic models and experiments should be

893   designed that incorporate mixtures of organic and inorganic ligands and analogue

894   mineral surfaces.

895

896   To summarise, the distinctive Fe and Mn enrichment of the paleo-water table samples

897   supports the suggestion of open system behaviour in this zone (Wimpenny et al.,

898   2007). The observed Zn and Cu enrichment could be explained by mobilisation from

899   zones II or IV of the weathering profile or an additional groundwater-borne source,

900 with scavenging on precipitating oxide phases. Specifically, we suggest that Cu and

901 Zn are primarily scavenged by a Mn oxide phase at 7.5m depth, consistent with

902 previously published Tl isotope evidence (Howarth et al., 2018).

903

904

905 **5.4 Synthesis: Cu and Zn isotopes in the weathering environment**

906

907 *5.4.1 Integrated weathering profiles and isotope fractionation during weathering*

908

909 To draw broader conclusions regarding the behaviour of Cu and Zn during

910 lateritization, and weathering in general, we compare integrated τ-values and isotopic

911 compositions from weathering and soil profiles from diverse localities. To facilitate

912 this comparison, we normalise weathered delta values to the presumed parent material

913 (where, e.g., $\Delta^{66}Zn = \delta^{66}Zn_{parent} - \delta^{66}Zn_{sample}$) and calculate integrated $\Delta^{66}Zn_{int}$ and

914 $\Delta^{65}Cu_{int}$ values (Table 2) for the entire weathering profile in the same fashion as used

915 to calculate integrated τ-values (Eqn. 6).

916

917 The SQ laterite profile shows an integrated loss of Zn of –23%, with an integrated

918 $\Delta^{66}Zn_{int}$ of –0.14‰ (Table 2). These SQ τ–Δ data are plotted alongside data from the

919 literature in Figure 9, updating the compilation in Moynier et al. (2017, their Fig. 11).

920 Overall, Zn-depleted (negative τ_{Zn}) weathering profiles and soils show limited isotope

921 fractionation from the parent lithology. However, at the highest degrees of chemical

922 weathering, above ~70% Zn depletion compared to the protolith, significant

923 preferential loss of heavy Zn isotopes in three different lateritic weathering profiles is

924 observed (from India: Suhr et al., 2018 and this study; from Cameroon: Viers et al.,

925 2007).

926

927 For Cu, a smaller integrated loss of –7% from the SQ profile is calculated, with a

928 more negative $\Delta^{65}Cu_{int}$ of –0.32‰ (Table 2). There is considerably more scatter in the

929 $\tau_{Cu} - \Delta^{65}Cu$ plot (Fig. 9B) – likely due to the multiple potential processes influencing

930 Cu isotopes and to more heterogeneous protolith Cu concentrations. However, nearly

931 all Cu-depleted profiles show negative $\Delta^{65}Cu_{int}$ values (plotting in the lower left

quadrant of Fig. 9B), indicating consistent loss of isotopically heavy Cu during weathering.

Two plausible explanations for the release of isotopically heavy Zn and Cu during lateritic weathering have been discussed: (1) incorporation of light isotopes in aluminous Fe oxide phases (ferrugination) or (2) organic complexation of heavy isotopes in the dissolved phase. In section 5.2.1, we suggested that organic complexation might lead to mobilization of heavy isotopes if mineral dissolution approaches chemical equilibrium, and that this scenario would be plausible in a transport-limited weathering regime. However, Figure 9 does not provide evidence for the converse prediction – of mobilization of light Cu (or Zn) isotopes in kinetically controlled, weathering-limited regimes (Fig. 9). Alternatively, in section 5.2.2, we suggested that organic complexation retains heavy isotopes in the aqueous phase *after* mobilization of Cu and Zn from their host mineral phases, with sorption of the complementary light pool on secondary Fe oxide minerals (section 5.2.2).

It is notable that Cu isotope data from weathering profiles developed on different lithologies fall on a similar fractionation trend (Fig. 9B, dashed arrow). Mathur et al. (2012) and Lv et al. (2016) favour oxidative weathering of Cu sulphides to explain residual isotopically light Cu signatures observed in weathered black shales. Given the absence of Cu-hosting sulphide phases in the SQ laterite, we propose that a combination of organic complexation in the aqueous phase and retention of light isotopes by secondary precipitating Fe oxide phases is the most likely explanation for the release of heavy Cu (and Zn) isotopes during lateritization. At greater degrees of Cu loss (>80%), Vance et al. (2016) observe a return towards protolith Cu isotope compositions in a sequence of increasingly waterlogged basaltic soils in Hawaii (Fig. 9B, dotted arrow), which they attribute to reduction of Fe oxides and return of the associated isotopically light Cu to the aqueous phase.

5.4.2 Implications for the weathering-derived flux of Zn and Cu to rivers on geological timescales

The sensitivity of the global cycles of Zn and Cu to a change in the riverine flux depends on the magnitude and timescale of the change compared to the residence time

966   of the element in the ocean. In the modern ocean, both Zn and Cu have relatively

967   short residence times of a few thousand years (Hayes et al., 2018 and references

968   therein). Thus, there is scope to influence the global ocean budgets of Zn and Cu via a

969   change in the riverine input. There are two possible ways to influence the isotopic

970   composition of the weathering-derived input of Zn and Cu to rivers: (1) change the

971   isotopic composition of the predominant weathered lithology and (2) change the

972   intensity of weathering and any associated isotope fractionation. The former is

973   unlikely to be a major control, because clastic sediments and igneous rocks have

974   restricted Zn and Cu isotope compositions (Moynier et al., 2017) and because there is

975   no consistent relationship between riverine δ^{66}Zn or δ^{65}Cu and catchment lithology in

976   modern dissolved phase river data (Vance et al., 2008; Little et al., 2014b). In this

977   contribution, we set out to address the latter, i.e. what is the maximum leverage of

978   chemical weathering on the isotopic composition of Zn and Cu supplied to rivers?

979

980   Figure 9A illustrates that significant weathering-derived Zn isotope fractionation only

981   occurs during extreme chemical weathering (lateritization). Lateritization was

982   promoted during Greenhouse climate periods of Earth history (e.g., the mid Miocene

983   Climatic Optimum), with the mid Tertiary to mid Quaternary considered to be a

984   period of particularly intensive chemical weathering (e.g., Dalvi et al., 2004; Thorne

985   et al., 2012; Widdowson, 2009). Could such a shift in weathering style have an impact

986   on the riverine δ^{66}Zn signature? While our data indicate that the Zn isotope

987   composition of the instantaneous flux to rivers from lateritic terrains can change, we

988   suggest that even widespread lateritization is unlikely to have had a major impact on

989   global average riverine δ^{66}Zn. At the very high degrees of Zn mobility observed

990   during lateritic weathering, the isotopic composition of the cumulative aqueous phase

991   will approach that of the protolith by mass balance. Thus, the average Zn isotope

992   composition of the source of Zn to rivers should be rather insensitive to climate-

993   driven change on geological timescales. Nevertheless, the scope for an instantaneous

994   change in the riverine flux should be considered on short timescales and at local and

995   regional spatial scales.

996

997   The small but growing dataset for Cu isotopes during weathering indicates release of

998   isotopically heavy Cu in all oxygenated environments (Fig. 9B), consistent with the

999   observed isotopically heavy Cu in the dissolved phase of modern rivers (Vance et al.,

1000 2008). In contrast, weathering in modern reducing environments appears to re-release

1001 isotopically light Cu associated with Fe-Mn oxides (Fig. 9B; Vance et al., 2016).

1002 Periodic flooding may also lead to reduction of Cu(II) to Cu(I), with release of

1003 isotopically light Cu(I) to the aqueous phase (Bigalke et al., 2010c; Bigalke et al.,

1004 2013; Babcsányi et al., 2014). Generally, however, Cu mobility during chemical

1005 weathering is likely to be significantly reduced under anoxic conditions (e.g., Neaman

1006 et al., 2005a, 2005b). Copper and Cu isotopes may therefore be an interesting marker

1007 for the presence or absence of oxygen during the development of paleosols.

1008

1009 Finally, release of isotopically heavy Cu during weathering is consistent with the

1010 scenario outlined by Chi Fru et al. (2016) for an observed shift from relatively low to

1011 higher δ^{65}Cu values in marine sediments across the great oxidation event (GOE). This

1012 shift was interpreted to reflect release of isotopically heavy Cu from the continents on

1013 the establishment of oxidative weathering (Chi Fru et al., 2016). These authors

1014 favoured oxidative weathering of sulphides as the primary mechanism responsible for

1015 releasing heavy Cu, while our study emphasizes that weathering in an oxygenated

1016 environment promotes retention of light Cu and release of heavy Cu, regardless of the

1017 primary host phase.

1018

1019 **6.0 Conclusions**

1020

1021 We have presented evidence of systematic and correlated Zn and Cu isotope

1022 fractionation during lateritization, observing retention of light isotopes in the

1023 associated weathering profile. Zinc and Cu in the residue are likely incorporated in

1024 secondary aluminous Fe oxide phases in the laterite, a process of 'ferrugination' that

1025 may itself be accompanied by isotope fractionation. Alternatively, the precipitating Fe

1026 oxide phases may passively scavenge light isotopes due to preferential organic

1027 complexation of heavy isotopes in the aqueous phase. The relative roles of organic

1028 complexation versus incorporation in Fe oxide phases, and their interaction with the

1029 multitude of other controls on metal speciation in the weathering environment (e.g.,

1030 presence of inorganic ligands, pH, redox, solid organic matter) are an important target

1031 for future experimental and theoretical work.

1032

1033 Our study, taken together with those previously published, illustrates that Zn isotope

1034 fractionation during weathering is limited, except at very extreme degrees of Zn

1035 removal. Therefore, mass balance constraints limit the impact of isotopic fractionation

1036 at high degrees of chemical weathering on the δ^{66}Zn of the riverine flux. This

1037 inference is consistent with the modern measured average δ^{66}Zn in rivers, which is

1038 unfractionated from the lithogenic δ^{66}Zn value.

1039

1040 In contrast, weathering of all lithologies studied to date appears to be associated with

1041 preferential retention of isotopically light Cu, consistent with isotopically heavy Cu in

1042 the dissolved pool of rivers. Weathering alone cannot account for the isotopically

1043 heavy riverine flux on long timescales, however, due to the relatively small pool of

1044 light Cu stored in terrestrial reservoirs like soils (Vance et al., 2016). Likely, the

1045 processes responsible for the liberation of heavy Cu during weathering (or,

1046 conversely, the retention of light Cu) continue to operate in some form downstream,

1047 with partitioning between the dissolved and particulate phase maintained in rivers and

1048 the oceans.

1049

1050

1062

1063 **Figure Captions**

1064

1065 **Figure 1**. **Left**: The location of Goa state (red) on the Indian Dharwar Craton

1066 (adapted from Paton et al., 2007). In the northeastern corner of the state, Deccan Trap

1067 flood basalts overlie the Dharwar metasediments. **Right**: The geology of Goa state

1068 (adapted from Widdowson, 2009; Devaraju et al., 2010). The black dashed line

1069 represents the state boundary. The Merces Quarry (SQ) laterite profile (labelled) is

1070 located at 15°28'44"N, 73°52'35"E. It is developed on Dharwar Late Archaean

1071 biotite-bearing greywacke.

1072

1073 **Figure 2.** Left: Schematic illustrating the depth distribution of samples in the laterite

1074 profile in relation to characteristic zones of alteration (Wimpenny et al., 2007;

1075 Widdowson, 2009). Graphs from left to right: Major element concentration variations

1076 (SiO_2, Al_2O_3, Fe_2O_3; Widdowson, 2009), MnO concentration variations (Widdowson,

1077 2009), and indices of alteration (Chemical Index of Alteration, CIA; Index of

1078 Lateritization, IOL; see text for further details). Grey shading highlights zone III, the

1079 paleo-water table. Samples showing only limited alteration, from below the dotted

1080 line of seepage (zone I), are paler in colour.

1081

1082 **Figure 3.** The crystal abundances of major mineral phases in the SQ laterite

1083 weathering profile compared to the four identified zones of alteration (Fig. 2;

1084 Wimpenney et al., 2007).

1085

1086 **Figure 4. A.** Concentration profiles and **B.** τ enrichment-depletion profiles (see text

1087 for details) of Li (grey triangles), Zn (red squares) and Cu (blue diamonds) in the SQ

1088 profile. C. τ enrichment-depletion profiles for Fe and Mn. Open symbols: little

1089 altered samples in zone I, below line of seepage (dotted line). Filled symbols: altered

1090 samples in zones II-IV, above line of seepage. Grey shaded zone III has been

1091 influenced by the paleo-water table.

1092

1093 **Figure 5. A.** Depth profiles of $\delta^{66}Zn$ (red squares) and $\delta^{65}Cu$ (blue diamonds). Open

1094 symbols: unaltered-little altered samples in zone I, below line of seepage (dotted line).

1095 Filled symbols: very increasingly altered zone II-IV mottled and lateritic samples.

1096   Shaded grey rectangle: zone III, influenced by the paleo-water table. **B.** Positive

1097   correlation between $\delta^{66}Zn$ and $\delta^{65}Cu$ in the SQ profile. Linear regression (arrow)

1098   indicates coupled loss of heavy Cu and Zn isotopes during lateritization and a

1099   resultant shift towards residual isotopically light values. Error bars represent long-

1100   term external 2SD reproducibility.

1101

1102   **Figure 6**. Covariation of Zn and Cu with selected major (A-D) and trace elements (E-

1103   H) in samples from zone I (unaltered – little altered) of the SQ laterite profile.

1104   Positive correlations of Zn with elements commonly hosted in biotite (Mg, K, Li, Co

1105   and Rb) suggest that Zn is primarily hosted in biotite in the parent greywacke (see

1106   also Fig. S3). Copper shows negative correlations with most other major and trace

1107   elements, with the exception of SiO_2 and Na_2O (Panel D), suggesting an association

1108   with a detrital phase.

1109

1110   **Figure 7.** Rayleigh fractionation modelling of **A.** Zn and **B.** Cu isotopes assuming

1111   preferential mobilization of heavy isotopes to the dissolved phase, assuming $R = R_0 \cdot f$

1112 $^{\alpha-1}$ (where R_0 is the isotope ratio of the protolith (larger open symbols), f the fraction

1113   removed and α the fractionation factor. For Zn: $\alpha = 1.0002$, for Cu: $\alpha = 1.001$).

1114   Dashed line: residual isotopic composition of the solid. Dash-dotted line: cumulative

1115   isotopic composition of the fluid removed from the system. Dotted line: instantaneous

1116   fluid isotopic composition. Symbols as in Figures 4 and 6. Error bars represent long-

1117   term external 2SD reproducibility. Paleo-water table sample SQ11 labelled.

1118

1119   **Figure 8.** Negative correlations of $\delta^{66}Zn$ (red squares) and $\delta^{65}Cu$ (blue diamonds)

1120   with Fe_2O_3 in the SQ profile. Paleo-water table sample SQ11 circled, other symbols

1121   as in Figure 4. Regressions are shown excluding (solid lines) and including (dashed

1122   lines) SQ11. Error bars represent long-term external 2SD reproducibility.

1123

1124   **Figure 9.** Integrated τ and integrated isotopic compositions for global weathering

1125   profiles **A**. Zn and **B**. Cu. Note, data are only included for studies where τ values are

1126   reported or can be calculated (Viers et al., 2007; Mathur et al., 2012; Liu et al., 2014;

1127   Lv et al., 2016; Vance et al., 2016). In order to include as much data as possible, but

1128   where an integrated τ-value cannot be calculated because horizon depths are not

1129   reported, either the full profile (for the central China black shale; Lv et al., 2016) or

1130   the mean and 1SD for each published profile (for the Cameroon laterite profiles; Viers

1131   et al., 2007) is shown. The SQ laterite dataset is shown as a full profile and as an

1132   integrated signature (larger symbol). Recently published full profile Zn isotope data is

1133   also included for the Bidar laterite, developed on Deccan basalt, for comparison (Zn

1134   only: Suhr et al., 2018). Literature data: [1] Viers et al. (2007), [2] Suhr et al. (2018),

1135   [3] Vance et al. (2016), [4] Lv et al. (2016), [5] Liu et al. (2014), [6] Mathur et al.

1136   (2012).

1137

1138

References

Aleva G. J. (1984) Lateritization, bauxitization and cyclic landscape development in the Guiana Shield. *Bauxite*, 297–318.

Amrhein C. and Suarez D. L. (1988) The use of a surface complexation model to describe the kinetics of ligand-promoted dissolution of anorthite. *Geochim. Cosmochim. Acta*.

Anand R. R. and Gilkes R. J. (1987) Iron oxides in lateritic soils from Western Australia. *Eur. J. Soil Sci.* **38**, 607–622.

Aplin A. C. and Cronan D. S. (1985) Ferromanganese oxide deposits from the Central Pacific Ocean, I. Encrustations from the Line Islands Archipelago. *Geochim. Cosmochim. Acta* **49**, 427–436.

Archer C. and Vance D. (2004) Mass discrimination correction in multiple-collector plasma source mass spectrometry: an example using Cu and Zn isotopes. *J. Anal. At. Spectrom.* **19**, 656. Available at: http://xlink.rsc.org/?DOI=b315853e.

Archer C. and Vance D. (2008) The isotopic signature of the global riverine molybdenum flux and anoxia in the ancient oceans. *Nat. Geosci.* **1**, 597–600.

Argast S. and Donnelly T. W. (1986) Compositions and sources of metasediments in the upper Dharwar Supergroup, South India. *J. Geol.* **94**, 215–231.

Arnold T., Schönbächler M., Rehkämper M., Dong S., Zhao F. J., Kirk G. J. D., Coles B. J. and Weiss D. J. (2010) Measurement of zinc stable isotope ratios in biogeochemical matrices by double-spike MC-ICPMS and determination of the isotope ratio pool available for plants from soil. *Anal. Bioanal. Chem.* **398**, 3115–3125.

Babcsányi I., Imfeld G., Granet M. and Chabaux F. (2014) Copper stable isotopes to trace copper behavior in wetland systems. *Environ. Sci. Technol.* **48**, 5520–5529.

Babechuk M. G., Widdowson M. and Kamber B. S. (2014) Quantifying chemical weathering intensity and trace element release from two contrasting basalt profiles, Deccan Traps, India. *Chem. Geol.* **363**, 56–75. Available at: http://dx.doi.org/10.1016/j.chemgeo.2013.10.027.

Balistrieri L. S., Borrok D. M., Wanty R. B. and Ridley W. I. (2008) Fractionation of Cu and Zn isotopes during adsorption onto amorphous Fe(III) oxyhydroxide: Experimental mixing of acid rock drainage and ambient river water. *Geochim. Cosmochim. Acta* **72**, 311–328.

1172 Balistrieri L. S. and Murray J. W. (1986) The surface chemistry of sediments from the

1173   Panama Basin: The influence of Mn oxides on metal adsorption. *Geochim.*

1174   *Cosmochim. Acta* **50**, 2235–2243.

1175 Banks N. G. (1973) Biotite as a source of some of the sulfur in porphyry copper

1176   deposits. *Econ. Geol.* **68**, 697–703.

1177 Becker K., Catalano J. and Moynier F. (2014) Connecting Zinc Partitioning and

1178   Isotope Fractionation during Fe(II)-Catalyzed Recrystallization of Fe(III) Oxide

1179   Minerals. In *Goldschmidt Abstracts* p. 151.

1180 Benedetti M. F., Milne C. J., Kinniburgh D. G., Van Riemsdijk W. H. and Koopal L.

1181   K. (1995) Metal Ion Binding to Hemic Substances: Application of the Non-Ideal

1182   Competitive Adsorption Model. *Environ. Sci. Technol.* **29**, 446–457.

1183 Bennett P. C. (1991) Quartz dissolution in organic-rich aqueous systems. *Geochim.*

1184   *Cosmochim. Acta*.

1185 Bentahila Y., Othman D. Ben and Luck J.-M. (2008) Strontium, lead and zinc

1186   isotopes in marine cores as tracers of sedimentary provenance: A case study

1187   around Taiwan orogen. *Chem. Geol.* **248**, 62–82.

1188 Berthelin J. and Munier-Lamy C. (1983) Microbial Mobilization and Preconcentration

1189   of Uranium from Various Rock Materials by Fungi. *Ecol. Bull.*, 395–401.

1190   Available at: http://www.jstor.org/stable/20112875.

1191 Bigalke M., Kersten M., Weyer S. and Wilcke W. (2013) Isotopes trace

1192   biogeochemistry and sources of Cu and Zn in an intertidal soil. *Soil Sci. Soc. Am.*

1193   *J.* **77**, 680–691.

1194 Bigalke M., Weyer S., Kobza J. and Wilcke W. (2010a) Stable Cu and Zn isotope

1195   ratios as tracers of sources and transport of Cu and Zn in contaminated soil.

1196   *Geochim. Cosmochim. Acta* **74**, 6801–6813. Available at:

1197   http://dx.doi.org/10.1016/j.gca.2010.08.044.

1198 Bigalke M., Weyer S. and Wilcke W. (2010b) Copper isotope fractionation during

1199   complexation with insolubilized humic acid. *Environ. Sci. Technol.* **44**, 5496–

1200   5502.

1201 Bigalke M., Weyer S. and Wilcke W. (2010c) Stable copper isotopes: A novel tool to

1202   trace copper behavior in hydromorphic soils. *Soil Sci. Soc. Am. J.* **74**, 60.

1203 Bigalke M., Weyer S. and Wilcke W. (2011) Stable Cu isotope fractionation in soils

1204   during oxic weathering and podzolization. *Geochim. Cosmochim. Acta* **75**, 3119–

1205   3134. Available at: http://dx.doi.org/10.1016/j.gca.2011.03.005.

1206 Bonnet N. J., Beauvais A., Arnaud N., Chardon D. and Jayananda M. (2014)
1207   First40Ar/39Ar dating of intense Late Palaeogene lateritic weathering in
1208   Peninsular India. *Earth Planet. Sci. Lett.* **386**, 126–137. Available at:
1209   http://dx.doi.org/10.1016/j.epsl.2013.11.002.

1210 Borrok D. M., Nimick D. A., Wanty R. B. and Ridley W. I. (2008) Isotopic variations
1211   of dissolved copper and zinc in stream waters affected by historical mining.
1212   *Geochim. Cosmochim. Acta* **72**, 329–344.

1213 Brantley S. L. (2003) Reaction Kinetics of Primary Rock-forming Minerals under
1214   Ambient Conditions. In *Treatise on Geochemistry* (eds. H. D. Holland and K. K.
1215   Turekian). Elsevier. pp. 73–117.

1216 Brantley S. L. and Lebedeva M. (2011) Learning to Read the Chemistry of Regolith
1217   to Understand the Critical Zone. *Annu. Rev. Earth Planet. Sci.* **39**, 387–416.
1218   Available at: http://www.annualreviews.org/doi/10.1146/annurev-earth-040809-
1219   152321.

1220 Brantley S. L., Liermann L. and Bullen T. D. (2001) Fractionation of Fe isotopes by
1221   soil microbes and organic acids. *Geology*.

1222 Brantley S. L., Liermann L. J., Guynn R. L., Anbar A., Icopini G. A. and Barling J.
1223   (2004) Fe isotopic fractionation during mineral dissolution with and without
1224   bacteria. *Geochim. Cosmochim. Acta* **68**, 3189–3204.

1225 Bridgestock L. J., Williams H., Rehkämper M., Larner F., Giscard M. D., Hammond
1226   S., Coles B., Andreasen R., Wood B. J. and Theis K. J. (2014) Unlocking the
1227   zinc isotope systematics of iron meteorites. *Earth Planet. Sci. Lett.* **400**, 153–
1228   164.

1229 Bruland K. W. (1989) Complexation of zinc by natural organic ligands in the central
1230   North Pacific. *Limnol. Oceanogr.* **34**, 269–285.

1231 Bryan A. L., Dong S., Wilkes E. B. and Wasylenki L. E. (2015) Zinc isotope
1232   fractionation during adsorption onto Mn oxyhydroxide at low and high ionic
1233   strength. *Geochim. Cosmochim. Acta* **157**, 182–197. Available at:
1234   http://dx.doi.org/10.1016/j.gca.2015.01.026.

1235 Cameron V. and Vance D. (2014) Heavy nickel isotope compositions in rivers and the
1236   oceans. *Geochim. Cosmochim. Acta* **128**, 195–211. Available at:
1237   http://dx.doi.org/10.1016/j.gca.2013.12.007.

1238 Catts J. G. and Langmuir D. (1986) Adsorption of Cu, Pb and Zn by δMnO2:
1239   applicability of the site binding-surface complexation model. *Appl.*

Geochemistry **1**, 255–264.

Chadwick O. A., Brimhall G. H. and Hendricks D. M. (1990) From a black to a gray box—a mass balance interpretation of pedogenesis. *Geomorphology* **3**, 369–390.

Chapman J. B., Weiss D. J., Shan Y. and Lemburger M. (2009) Iron isotope fractionation during leaching of granite and basalt by hydrochloric and oxalic acids. *Geochim. Cosmochim. Acta*.

Chi Fru E., Rodríguez N. P., Partin C. A., Lalonde S. V., Andersson P., Weiss D. J., El Albani A., Rodushkin I. and Konhauser K. O. (2016) Cu isotopes in marine black shales record the Great Oxidation Event. *Proc. Natl. Acad. Sci.* **113**, 4941–4946. Available at: http://www.pnas.org/lookup/doi/10.1073/pnas.1523544113.

Coale K. H. and Bruland K. W. (1988) Copper complexation in the Northeast Pacific. *Limnol. Oceanogr.* **33**, 1084–1101.

Cornell R. M. and Giovanoli R. (1988) The influence of copper on the transformation of ferrihydrite (5Fe2O3· 9H2O) into crystalline products in alkaline media. *Polyhedron* **7**, 385–391.

Cornell R. M. and Schwertmann U. (2003) *The iron oxides: structure, properties, reactions, occurrences and uses.*, John Wiley & Sons.

Coutaud A., Meheut M., Viers J., Rols J. L. and Pokrovsky O. S. (2014) Zn isotope fractionation during interaction with phototrophic biofilm. *Chem. Geol.* **390**, 46–60. Available at: http://dx.doi.org/10.1016/j.chemgeo.2014.10.004.

Coutaud M., Méheut M., Glatzel P., Pokrovski G. S., Viers J., Rols J. L. and Pokrovsky O. S. (2018) Small changes in Cu redox state and speciation generate large isotope fractionation during adsorption and incorporation of Cu by a phototrophic biofilm. *Geochim. Cosmochim. Acta* **220**, 1–18.

Dalvi A. D., Bacon W. G. and Osborne R. C. (2004) The Past and the Future of Nickel Laterites. *PDAC 2004 Int. Conv.*, 1–27.

Deer W. A., Howie R. A. and Zussman J. (1992) *An introduction to the rock-forming minerals.*, Longman Scientific & Technical Hong Kong.

Dessai A. G. (2011) The geology of Goa Group: Revisited. *J. Geol. Soc. India* **78**, 233–242.

Devaraju T. C., Sudhakara T. L., Kaukonen R. J., Viljoen R. P., Alapieti T. T., Ahmed S. A. and Sivakumar S. (2010) Petrology and geochemistry of greywackes from Goa-Dharwar sector, western Dharwar craton: Implications for volcanoclastic origin. *J. Geol. Soc. India* **75**, 465–487.

1274   Dideriksen K., Baker J. A. and Stipp S. L. S. (2008) Equilibrium Fe isotope

1275   fractionation between inorganic aqueous Fe(III) and the siderophore complex,

1276   Fe(III)-desferrioxamine B. *Earth Planet*. *Sci*. *Lett*. **269**, 280–290.

1277   Dong S., Weiss D. J., Strekopytov S., Kreissig K., Sun Y., Baker A. R. and Formenti

1278   P. (2013) Stable isotope ratio measurements of Cu and Zn in mineral dust (bulk

1279   and size fractions) from the Taklimakan Desert and the Sahel and in aerosols

1280   from the eastern tropical North Atlantic Ocean. *Talanta* **114**, 103–109. Available

1281   at: http://dx.doi.org/10.1016/j.talanta.2013.03.062.

1282   Doucet L. S., Laurent O., Mattielli N. and Debouge W. (2018) Zn isotope

1283   heterogeneity in the continental lithosphere: New evidence from Archean

1284   granitoids of the northern Kaapvaal craton, South Africa. *Chem*. *Geol*. **476**, 260–

1285   271. Available at: http://dx.doi.org/10.1016/j.chemgeo.2017.11.022.

1286   Ehrlich S., Butler I., Halicz L., Rickard D., Oldroyd A. and Matthews A. (2004)

1287   Experimental study of the copper isotope fractionation between aqueous Cu(II)

1288   and covellite, CuS. *Chem*. *Geol*. **209**, 259–269.

1289   Fernandez A. and Borrok D. M. (2009) Fractionation of Cu, Fe, and Zn isotopes

1290   during the oxidative weathering of sulfide-rich rocks. *Chem*. *Geol*. **264**, 1–12.

1291   Available at: http://dx.doi.org/10.1016/j.chemgeo.2009.01.024.

1292   Frei R., Poiré D. and Frei K. M. (2014) Weathering on land and transport of

1293   chromium to the ocean in a subtropical region (Misiones, NW Argentina): A

1294   chromium stable isotope perspective. *Chem*. *Geol*. **381**, 110–124. Available at:

1295   http://dx.doi.org/10.1016/j.chemgeo.2014.05.015.

1296   Fujii T. and Albarede F. (2012) Ab initio calculation of the Zn isotope effect in

1297   phosphates, citrates, and malates and applications to plants and soil. *PLoS One* **7**,

1298   0–4.

1299   Fujii T., Moynier F., Abe M., Nemoto K. and Albarède F. (2013) Copper isotope

1300   fractionation between aqueous compounds relevant to low temperature

1301   geochemistry and biology. *Geochim*. *Cosmochim*. *Acta* **110**, 29–44.

1302   Fujii T., Moynier F., Blichert-Toft J. and Albarède F. (2014) Density functional

1303   theory estimation of isotope fractionation of Fe, Ni, Cu, and Zn among species

1304   relevant to geochemical and biological environments. *Geochim*. *Cosmochim*.

1305   *Acta* **140**, 553–576.

1306   Gerth J. (1990) Unit-cell dimensions of pure and trace metal-associated goethites.

1307   *Geochim*. *Cosmochim*. *Acta* **54**, 363–371.

1308   Goldich S. S. (1938) A Study in Rock-Weathering. *J. Geol.*

1309   Gomez-Gonzalez M. A., Garcia-Guinea J., Laborda F. and Garrido F. (2015)
1310   Thallium occurrence and partitioning in soils and sediments affected by mining
1311   activities in Madrid province (Spain). *Sci. Total Environ.* **536**, 268–278.

1312   Goudie A. S. (2004) Laterite. *Encycl. Geomorphol.*

1313   Grybos M., Davranche M., Gruau G. and Petitjean P. (2007) Is trace metal release in
1314   wetland soils controlled by organic matter mobility or Fe-oxyhydroxides
1315   reduction? *J. Colloid Interface Sci.* **314**, 490–501.

1316   Guinoiseau D., Gélabert A., Allard T., Louvat P., Moreira-Turcq P. and Benedetti M.
1317   F. (2017) Zinc and copper behaviour at the soil-river interface: New insights by
1318   Zn and Cu isotopes in the organic-rich Rio Negro basin. *Geochim. Cosmochim.*
1319   *Acta* **213**, 178–197. Available at: http://dx.doi.org/10.1016/j.gca.2017.06.030.

1320   Guinoiseau D., Gélabert A., Moureau J., Louvat P. and Benedetti M. F. (2016) Zn
1321   Isotope Fractionation during Sorption onto Kaolinite. *Environ. Sci. Technol.* **50**,
1322   1844–1852.

1323   Harter R. D. and Naidu R. (1995) Role of metal-organic complexation in metal
1324   sorption by soils. *Adv. Agron.* **55**, 219–263.

1325   Hayes C. T., Anderson R. F., Cheng H., Conway T. M., Edwards R. L., Fleisher M.
1326   Q., Ho P., Huang K. F., John S. G., Landing W. M., Little S. H., Lu Y., Morton
1327   P. L., Moran S. B., Robinson L. F., Shelley R. U., Shiller A. M. and Zheng X. Y.
1328   (2018) Replacement Times of a Spectrum of Elements in the North Atlantic
1329   Based on Thorium Supply. *Global Biogeochem. Cycles* **32**, 1294–1311.

1330   Hibbert C. (2017) Controls on seasonal elemental variation in tropical rivers in Goa,
1331   India. Doctoral thesis, Birkbeck, University of London. Available at:
1332   http://bbktheses.da.ulcc.ac.uk/275/.

1333   Hoffmann S. R., Shafer M. M. and Armstrong D. E. (2007) Strong Colloidal and
1334   Dissolved Organic Ligands Binding Copper and Zinc in Rivers. **41**, 6996–7002.

1335   Howarth S., Prytulak J., Little S. H., Hammond S. J. and Widdowson M. (2018)
1336   Thallium concentration and thallium isotope composition of lateritic terrains.
1337   *Geochim. Cosmochim. Acta* **239**, 446–462.

1338   Huh Y., Chan L. H., Zhang L. and Edmond J. M. (1998) Lithium and its isotopes in
1339   major world rivers: implications for weathering and the oceanic budget.
1340   *Geochim. Cosmochim. Acta* **62**, 2039–2051.

1341   Ijichi Y., Ohno T. and Sakata S. (2018) Copper isotopic fractionation during

1342   adsorption on manganese oxide: Effects of pH and desorption. *Geochem. J.* **52**,

1343   e1–e6.

1344 Isson T. T., Love G. D., Dupont C. L., Reinhard C. T., Zumberge A. J., Asael D.,

1345   Gueguen B., McCrow J., Gill B. C., Owens J., Rainbird R. H., Rooney A. D.,

1346   Zhao M. Y., Stueeken E. E., Konhauser K. O., John S. G., Lyons T. W. and

1347   Planavsky N. J. (2018) Tracking the rise of eukaryotes to ecological dominance

1348   with zinc isotopes. *Geobiology* **16**, 341–352.

1349 John S. G., Kunzmann M., Townsend E. J. and Rosenberg A. D. (2017) Zinc and

1350   cadmium stable isotopes in the geological record: A case study from the post-

1351   snowball Earth Nuccaleena cap dolostone. *Palaeogeogr. Palaeoclimatol.*

1352   *Palaeoecol.* **466**, 202–208. Available at:

1353   http://dx.doi.org/10.1016/j.palaeo.2016.11.003.

1354 Jouvin D., Louvat P., Juillot F., Maréchal C. N. and Benedetti M. F. (2009) Zinc

1355   isotopic fractionation: Why organic matters. *Environ. Sci. Technol.* **43**, 5747–

1356   5754.

1357 Juillot F., Maréchal C., Ponthieu M., Cacaly S., Morin G., Benedetti M., Hazemann J.

1358   L., Proux O. and Guyot F. (2008) Zn isotopic fractionation caused by sorption on

1359   goethite and 2-Lines ferrihydrite. *Geochim. Cosmochim. Acta* **72**, 4886–4900.

1360 Kimball B. E., Mathur R., Dohnalkova A. C., Wall A. J., Runkel R. L. and Brantley

1361   S. L. (2009) Copper isotope fractionation in acid mine drainage. *Geochim.*

1362   *Cosmochim. Acta* **73**, 1247–1263. Available at:

1363   http://dx.doi.org/10.1016/j.gca.2008.11.035.

1364 Koschinsky A. and Hein J. R. (2003) Uptake of elements from seawater by

1365   ferromanganese crusts: Solid-phase associations and seawater speciation. *Mar.*

1366   *Geol.* **198**, 331–351.

1367 Kump L. R., Brantley S. L. and Arthur M. A. (2000) Chemical Weathering,

1368   Atomspheric CO2, and Climate. *Annu. Rev. Earth Planet. Sci.* **28**, 611–667.

1369 Kunzmann M., Halverson G. P., Sossi P. A., Raub T. D., Payne J. L. and Kirby J.

1370   (2013) Zn isotope evidence for immediate resumption of primary productivity

1371   after snowball Earth. *Geology* **41**, 27–30.

1372 Larner F. and Rehkämper M. (2012) Evaluation of Stable Isotope Tracing for ZnO

1373   Nanomaterials · New Constraints from High Precision Isotope Analyses and

1374   Modeling. *Environ. Sci. Technol.* **46**, 4149–4158.

1375   Larner F., Rehkämper M., Coles B. J., Kreissig K., Weiss D. J., Sampson B.,

1376   Unsworth C. and Strekopytov S. (2011) A new separation procedure for Cu prior

1377   to stable isotope analysis by MC-ICP-MS. *J. Anal. At. Spectrom.* **26**, 1627–1632.

1378   Lebedeva M. I., Fletcher R. C. and Brantley S. L. (2010) A mathematical model for

1379   steady-state regolith production at constant erosion rate. *Earth Surf. Process.*

1380   *Landforms* **35**, 508–524.

1381   Little S. H., Sherman D. M., Vance D. and Hein J. R. (2014a) Molecular controls on

1382   Cu and Zn isotopic fractionation in Fe-Mn crusts. *Earth Planet. Sci. Lett.* **396**,

1383   213–222.

1384   Little S. H., Vance D., Walker-Brown C. and Landing W. M. (2014b) The oceanic

1385   mass balance of copper and zinc isotopes, investigated by analysis of their

1386   inputs, and outputs to ferromanganese oxide sediments. *Geochim. Cosmochim.*

1387   *Acta* **125**, 673–693.

1388   Liu S. A., Teng F. Z., Li S., Wei G. J., Ma J. L. and Li D. (2014) Copper and iron

1389   isotope fractionation during weathering and pedogenesis: Insights from saprolite

1390   profiles. *Geochim. Cosmochim. Acta* **146**, 59–75. Available at:

1391   http://dx.doi.org/10.1016/j.gca.2014.09.040.

1392   Lupker M., France-Lanord C., Lavé J., Bouchez J., Galy V., Métivier F., Gaillardet J.,

1393   Lartiges B. and Mugnier J. L. (2011) A Rouse-based method to integrate the

1394   chemical composition of river sediments: Application to the Ganga basin. *J.*

1395   *Geophys. Res. Earth Surf.* **116**, 1–24.

1396   Lv Y., Liu S. A., Zhu J. M. and Li S. (2016) Copper and zinc isotope fractionation

1397   during deposition and weathering of highly metalliferous black shales in central

1398   China. *Chem. Geol.* **445**, 24–35. Available at:

1399   http://dx.doi.org/10.1016/j.chemgeo.2016.01.016.

1400   Manceau a, Schlegel M. ., Musso M., Sole V. ., Gauthier C., Petit P. . and Trolard F.

1401   (2000) Crystal chemistry of trace elements in natural and synthetic goethite.

1402   *Geochim. Cosmochim. Acta* **64**, 3643–3661.

1403   Manceau A., Lanson B. and Drits V. A. (2002) Structure of heavy metal sorbed

1404   birnessite. Part III: Results from powder and polarized extended X-ray

1405   absorption fine structure spectroscopy. *Geochim. Cosmochim. Acta* **66**, 2639–

1406   2663.

1407   Maréchal C. and Albarède F. (2002) Ion-exchange fractionation of copper and zinc

1408   isotopes. *Geochim. Cosmochim. Acta* **66**, 1499–1509.

1409   Maréchal C. N., Télouk P. and Albarède F. (1999) Precise analysis of copper and zinc

1410   isotopic compositions by plasma-source mass spectrometry. *Chem. Geol.* **156**,

1411   251–273.

1412   Marković T., Manzoor S., Humphreys-Williams E., Kirk G. J. D., Vilar R. and Weiss

1413   D. J. (2017) Experimental Determination of Zinc Isotope Fractionation in

1414   Complexes with the Phytosiderophore 2′-Deoxymugeneic Acid (DMA) and Its

1415   Structural Analogues, and Implications for Plant Uptake Mechanisms. *Environ.*

1416   *Sci. Technol.* **51**, 98–107.

1417   Mathur R., Jin L., Prush V., Paul J., Ebersole C., Fornadel A., Williams J. Z. and

1418   Brantley S. (2012) Cu isotopes and concentrations during weathering of black

1419   shale of the Marcellus Formation, Huntingdon County, Pennsylvania (USA).

1420   *Chem. Geol.* **304–305**, 175–184. Available at:

1421   http://dx.doi.org/10.1016/j.chemgeo.2012.02.015.

1422   Mathur R., Ruiz J., Titley S., Liermann L., Buss H. and Brantley S. (2005) Cu

1423   isotopic fractionation in the supergene environment with and without bacteria.

1424   *Geochim. Cosmochim. Acta* **69**, 5233–5246.

1425   McBride M. B. (1981) Forms and distribution of copper in solid and solution phases

1426   of soil. In *Copper in Soils and Plants* (eds. J. F. Loneragan, A. D. Robson, and

1427   R. D. Graham). Academic Press: Australia.

1428   McBride M., Sauvé S., Hendershot W., Sauve S. and Hendershot W. (1997)

1429   Solubility control of Cu, Zn, Cd and Pb in contaminated soils. *Eur. J. Soil Sci.*

1430   **48**, 337–346.

1431   McFarlane M. J. (1983) Laterites. In *Chemical sediments and geomorphology*

1432   McFarlane M. J. (1976) Morphological mapping in laterite areas. *Stud. Geogr. Brno.*

1433   Moeller K., Schoenberg R., Pedersen R. B., Weiss D. and Dong S. (2012) Calibration

1434   of the New Certified Reference Materials ERM-AE633 and ERM-AE647 for

1435   Copper and IRMM-3702 for Zinc Isotope Amount Ratio Determinations.

1436   *Geostand. Geoanalytical Res.* **36**, 177–199.

1437   Moffett J. W. and Brand L. E. (1996) Production of strong, extracellular Cu chelators

1438   by marine cyanobacteria in response to Cu stress. *Limnol. Oceanogr.* **41**, 388–

1439   395.

1440   Morgan J. L. L., Wasylenki L. E., Nuester J. and Anbar A. D. (2010) Fe isotope

1441   fractionation during equilibration of Fe-organic complexes. *Environ. Sci.*

1442   *Technol.* **44**, 6095–6101.

1443   Moynier F., Vance D., Fujii T. and Savage P. (2017) The Isotope Geochemistry of
1444   Zinc and Copper. *Rev. Mineral. Geochemistry* **82**, 543–600. Available at:
1445   http://rimg.geoscienceworld.org/lookup/doi/10.2138/rmg.2017.82.13.

1446   Neaman A., Chorover J. and Brantley S. L. (2005a) Element mobility patterns record
1447   organic ligands in soils on early Earth. *Geology* **33**, 117–120.

1448   Neaman A., Chorover J. and Brantley S. L. (2005b) Implications of the evolution of
1449   organic acid moieties for basalt weathering over geological time. *Am. J. Sci.* **305**,
1450   147–185.

1451   Nesbitt H. W. and Young G. M. (1982) Early proterozoic climates and plate motions
1452   inferred from major element chemistry of lutites. *Nature*.

1453   Neubert N., Heri A. R., Voegelin A. R., Nägler T. F., Schlunegger F. and Villa I. M.
1454   (2011) The molybdenum isotopic composition in river water: Constraints from
1455   small catchments. *Earth Planet. Sci. Lett.* **304**, 180–190. Available at:
1456   http://dx.doi.org/10.1016/j.epsl.2011.02.001.

1457   Newbold T. J. (1844) Notes chiefly geological, across the Peninsula from
1458   Masultipatam to Goa, comprising remarks on the origin of regur and laterite:
1459   Occurrence of manganese veins in the latter and on certain traces of aqueous
1460   denudation on the surface of southern India. *J. Asiat. Soc. Beng.* **15**, 204–213.

1461   Nielsen S. G., Rehkämper M., Baker J. and Halliday A. N. (2004) The precise and
1462   accurate determination of thallium isotope compositions and concentrations for
1463   water samples by MC-ICPMS. *Chem. Geol.* **204**, 109–124.

1464   Opfergelt S., Cornélis J. T., Houben D., Givron C., Burton K. W. and Mattielli N.
1465   (2017) The influence of weathering and soil organic matter on Zn isotopes in
1466   soils. *Chem. Geol.* **466**, 140–148. Available at:
1467   http://dx.doi.org/10.1016/j.chemgeo.2017.06.002.

1468   Pascoe K. H. (1950) *A manual of the geology of India and Burma, Vol. 1.*, Govt of
1469   India, New Dehli.

1470   Paton C., Hergt J. M., Phillips D., Woodhead J. D. and Shee S. R. (2007) New
1471   insights into the genesis of Indian kimberlites from the Dharwar Craton via in
1472   situ Sr isotope analysis of groundmass perovskite. *Geology* **35**, 1011–1014.

1473   Peacock C. L. and Sherman D. M. (2007) Sorption of Ni by birnessite: Equilibrium
1474   controls on Ni in seawater. *Chem. Geol.* **238**, 94–106.

1475   Pokrovsky O. S., Viers J., Emnova E. E., Kompantseva E. I. and Freydier R. (2008)
1476   Copper isotope fractionation during its interaction with soil and aquatic

1477   microorganisms and metal oxy(hydr)oxides: Possible structural control.

1478   *Geochim. Cosmochim. Acta* **72**, 1742–1757.

1479   Pokrovsky O. S., Viers J. and Freydier R. (2005) Zinc stable isotope fractionation

1480   during its adsorption on oxides and hydroxides. *J. Colloid Interface Sci.* **291**,

1481   192–200.

1482   Pons M. L., Fujii T., Rosing M., Quitté G., Télouk P. and Albarède F. (2013) A Zn

1483   isotope perspective on the rise of continents. *Geobiology* **11**, 201–214.

1484   Post J. E. (1999) Manganese oxide minerals: Crystal structures and economic and

1485   environmental significance. *Proc. Natl. Acad. Sci.*

1486   Roser B. P., Cooper R. A., Nathan S. and Tulloch A. J. (1996) Reconnaissance

1487   sandstone geochemistry, provenance, and tectonic setting of the lower Paleozoic

1488   terranes of the West Coast and Nelson, New Zealand. *New Zeal. J. Geol.*

1489   *Geophys.*

1490   Ross S. J., Franzmeier D. P. and Roth C. B. (1976) Mineralogy and chemistry of

1491   manganese oxides in some Indiana soils. *Soil Sci. Soc. Am. J.* **40**, 137–143.

1492   Ryan B. M., Kirby J. K., Degryse F., Scheiderich K. and McLaughlin M. J. (2014)

1493   Copper isotope fractionation during equilibration with natural and synthetic

1494   ligands. *Environ. Sci. Technol.* **48**, 8620–8626.

1495   Schellman W. (1983) Geochemical principles of lateritic nickel ore formation. *Proc.*

1496   *Int. Semin. Lateritisation Process.*, 119–135. Available at:

1497   http://ci.nii.ac.jp/naid/10003418711/en/ [Accessed October 23, 2018].

1498   Schmidt P. W., Prasad V. and Ramam P. K. (1983) Magnetic ages of some Indian

1499   laterites. *Palaeogeogr. Palaeoclimatol. Palaeoecol.* **44**, 185–202. Available at:

1500   https://www.sciencedirect.com/science/article/pii/0031018283901025 [Accessed

1501   January 24, 2018].

1502   Schnoor J. L. (1990) Kinetics of chemical weathering: a comparison of laboratory and

1503   field weathering rates. In *Aquatic Chemical Kinetics: Reaction Rates of*

1504   *Processes in Natural Waters* (ed. W. Stumm). Zurich: Swiss Fed. Inst. Technol.

1505   pp. 475–504.

1506   Shank G. C., Skrabal S. A., Whitehead R. F. and Kieber R. J. (2004) Strong copper

1507   complexation in an organic-rich estuary: the importance of allochthonous

1508   dissolved organic matter. *Mar. Chem.* **88**, 21–39.

1509   Sherman D. M. (2013) Equilibrium isotopic fractionation of copper during

1510   oxidation/reduction, aqueous complexation and ore-forming processes:

1511   Predictions from hybrid density functional theory. *Geochim. Cosmochim. Acta*

1512   **118**, 85–97. Available at: http://dx.doi.org/10.1016/j.gca.2013.04.030.

1513 Sherman D. M. and Peacock C. L. (2010) Surface complexation of Cu on birnessite

1514   (δ-MnO2): Controls on Cu in the deep ocean. *Geochim. Cosmochim. Acta* **74**,

1515   6721–6730. Available at: http://dx.doi.org/10.1016/j.gca.2010.08.042.

1516 Siebert C., Nagler T. F. and Kramers J. D. (2001) Determination of molybdenum

1517   isotope fractionation by double-spike multicollector inductively coupled plasma

1518   mass spectrometry. *Geochemistry, Geophys. Geosystems* **2**, 1032.

1519 Singh B. and Gilkes R. J. (1992) Properties and distribution of iron oxides and their

1520   association with minor elements in the soils of south- western Australia. *Eur. J.*

1521   *Soil Sci.* **43**, 77–98.

1522 Srinivasan R., Naqvi S. M., Raj B. U., Rao D. V. S., Balaram V. and Rao T. G. (1989)

1523   Geochemistry of the Archaean greywackes from the northwestern part of the

1524   Chitradurga schist belt, Dharwar Craton, South India-evidence for granitoid

1525   upper crust in the Archaean. *Geol. Soc. India* **34**, 505–516.

1526 Stevenson E. I., Fantle M. S., Das S. B., Williams H. M. and Aciego S. M. (2017) The

1527   iron isotopic composition of subglacial streams draining the Greenland ice sheet.

1528   *Geochim. Cosmochim. Acta* **213**, 237–254. Available at:

1529   http://dx.doi.org/10.1016/j.gca.2017.06.002.

1530 Suhr N., Schoenberg R., Chew D., Rosca C., Widdowson M. and Kamber B. S.

1531   (2018) Elemental and isotopic behaviour of Zn in Deccan basalt weathering

1532   profiles: Chemical weathering from bedrock to laterite and links to Zn deficiency

1533   in tropical soils. *Sci. Total Environ.* **619–620**, 1451–1463. Available at:

1534   https://doi.org/10.1016/j.scitotenv.2017.11.112.

1535 Swoboda-Colberg N. G. and Drever J. I. (1993) Mineral dissolution rates in plot-scale

1536   field and laboratory experiments. *Chem. Geol.* **105**, 51–69.

1537 Szynkiewicz A. and Borrok D. M. (2016) Isotope variations of dissolved Zn in the

1538   Rio Grande watershed, USA: The role of adsorption on Zn isotope composition.

1539   *Earth Planet. Sci. Lett.* **433**, 293–302.

1540 Tardy Y. (1997) *Petrology of laterites and tropical soils.*, A.A. Balkema, Rotterdam.

1541   Available at: https://www.cabdirect.org/cabdirect/abstract/19981913040.

1542 Tardy Y., Kobilsek B. and Paquet H. (1991) Mineralogical composition and

1543   geographical distribution of African and Brazilian periatlantic laterites. The

1544   influence of continental drift and tropical paleoclimates during the past 150

1545 million years and implications for India and Australia. *J. African Earth Sci. (and*
1546 *Middle East)* **12**, 283–295.

1547 Taylor G. and Eggleton R. A. (2001) *Regolith Geology and Geomorphology.*, John
1548 Wiley & Sons.

1549 Taylor R. M., McKenzie R. M. and Norrish K. (1964) The mineralogy and chemistry
1550 of manganese in some australian soils. *Aust. J. Soil Res.* **2**, 235–248.

1551 Telus M., Dauphas N., Moynier F., Tissot F. L. H., Teng F.-Z., Nabelek P. I.,
1552 Craddock P. R. and Groat L. A. (2012) Iron, zinc, magnesium and uranium
1553 isotopic fractionation during continental crust differentiation: The tale from
1554 migmatites, granitoids, and pegmatites. *Geochim. Cosmochim. Acta* **97**, 247–
1555 265.

1556 Tessier A., Fortin D., Belzile N., DeVitre R. R. and Leppard G. G. (1996) Metal
1557 sorption to diagenetic iron and manganese oxyhydroxides and associated organic
1558 matter: Narrowing the gap between field and laboratory measurements.
1559 *Geochim. Cosmochim. Acta* **60**, 387–404.

1560 Thorne R. L., Roberts S. and Herrington R. (2012) Climate change and the formation
1561 of nickel laterite deposits. *Geology* **40**, 331–334.

1562 Tokashiki Y., Dlxon J. B. and Golden D. C. (1986) Manganese Oxide Analysis in
1563 Soils by Combined X-ray Diffraction and Selective Dissolution Methods 1. *Soil*
1564 *Sci. Soc. Am. J.*

1565 Uzochukwu G. A. and Dixon J. B. (1986) Manganese oxide minerals in nodules of
1566 two soils of Texas and Alabama. *Soil Sci. Soc. Am. J.* **50**, 1358–1363.

1567 Vance D., Archer C., Bermin J., Perkins J., Statham P. J., Lohan M. C., Ellwood M. J.
1568 and Mills R. A. (2008) The copper isotope geochemistry of rivers and the
1569 oceans. *Earth Planet. Sci. Lett.* **274**, 204–213.

1570 Vance D., Matthews A., Keech A., Archer C., Hudson G., Pett-Ridge J. and
1571 Chadwick O. A. (2016) The behaviour of Cu and Zn isotopes during soil
1572 development: Controls on the dissolved load of rivers. *Chem. Geol.* **445**, 36–53.
1573 Available at: http://dx.doi.org/10.1016/j.chemgeo.2016.06.002.

1574 Vdović N., Bišćan J. and Juraĉić M. (1991) Relationship between specific surface
1575 area and some chemical and physical properties of particulates: study in the
1576 northern Adriatic. *Mar. Chem.* **36**, 317–328.

1577 Viers J., Oliva P., Nonell A., Gélabert A., Sonke J. E., Freydier R., Gainville R. and
1578 Dupré B. (2007) Evidence of Zn isotopic fractionation in a soil-plant system of a

pristine tropical watershed (Nsimi, Cameroon). *Chem. Geol.* **239**, 124–137.

Weiss D. J., Boye K., Caldelas C. and Fendorf S. (2014) Zinc Isotope Fractionation during Early Dissolution of Biotite Granite. *Soil Sci. Soc. Am. J.* **78**, 171. Available at: https://www.soils.org/publications/sssaj/abstracts/78/1/171.

Weiss D. J., Rausch N., Mason T. F. D., Coles B. J., Wilkinson J. J., Ukonmaanaho L., Arnold T. and Nieminen T. M. (2007) Atmospheric deposition and isotope biogeochemistry of zinc in ombrotrophic peat. *Geochim. Cosmochim. Acta* **71**, 3498–3517.

Welch S. A. and Ullman W. J. (1996) Feldspar dissolution in acidic and organic solutions: Compositional and pH dependence of dissolution rate. *Geochim. Cosmochim. Acta.*

Welch S. A. and Ullman W. J. (1993) The effect of organic acids on plagioclase dissolution rates and stoichiometry. *Geochim. Cosmochim. Acta.*

Welch S. A. and Ullman W. J. (2000) The temperature dependence of bytownite feldspar dissolution in neutral aqueous solutions of inorganic and organic ligands at low temperature (5-35°C). *Chem. Geol.*

Wells M. L., Kozelka P. B. and Bruland K. W. (1998) The complexation of "dissolved" Cu, Zn, Cd and Pb by soluble and colloidal organic matter in Narragansett Bay, RI. *Mar. Chem.* **62**, 203–217.

West A. J., Galy A. and Bickle M. (2005) Tectonic and climatic controls on silicate weathering. *Earth Planet. Sci. Lett.* **235**, 211–228.

White A. F. and Buss H. L. (2014) Natural Weathering Rates of Silicate Minerals. *Treatise on Geochemistry*, 115–155. Available at: https://www.sciencedirect.com/science/article/pii/B9780080959757005040?via %3Dihub [Accessed November 16, 2018].

Widdowson M. (2009) *Evolution of Laterite in Goa.*, Available at: http://oro.open.ac.uk/19793/.

Widdowson M. (2004) Ferricrete, Ferralitisation. In *Encyclopedia of Geomorphology* (ed. A. S. Goudie). Routledge, London. pp. 365–367.

Widdowson M. (2007) Laterite and Ferricrete. In *Geochemical Sediments and Landscapes* (eds. D. J. Nash and S. J. McLaren). Blackwell Publishing Ltd. pp. 46–94.

Widdowson M. (1997) Tertiary palaeosurfaces of the SW Deccan, Western India: implications for passive margin uplift. *Geol. Soc. London, Spec. Publ.* **120**, 221–

1613   248. Available at:

1614   http://sp.lyellcollection.org/lookup/doi/10.1144/GSL.SP.1997.120.01.15.

1615 Widdowson M. and Gunnell Y. (1999) *Lateritization, Geomorphology and*

1616   *Geodynamics of a Passive Continental Margin: The Konkan and Kanara*

1617   *Coastal Lowlands of Western Peninsular India.*,

1618 Wiederhold J. G., Kraemer S. M., Teutsch N., Borer P. M., Halliday A. N. and

1619   Kretzschmar R. (2006) Iron isotope fractionation during proton-promoted,

1620   ligand-controlled, and reductive dissolution of goethite. *Environ. Sci. Technol.*

1621   **40**, 3787–3793.

1622 Wimpenny J., Gannoun A., Burton K. W., Widdowson M., James R. H. and Gíslason

1623   S. R. (2007) Rhenium and osmium isotope and elemental behaviour

1624   accompanying laterite formation in the Deccan region of India. *Earth Planet.*

1625   *Sci. Lett.* **261**, 239–258.

1626 Xue H. Bin, Kistler D. and Sigg L. (1995) Competition of copper and zinc for strong

1627   ligands in a eutrophic lake. *Limnol. Oceanogr.* **40**, 1142–1152.

1628

Table 1

Table 1. Isotope data for USGS rock standards (mean and 2SD) analysed in this study (in grey) versus recommended (Moynier et al., 2017) or published values.

	$\delta^{66}Zn_{JMC\text{-}Lyon}$ (‰)	2SD	n	$\delta^{65}Cu_{SRM976}$ (‰)	2SD	n
BHVO-2	0.39	0.07	6	0.07	0.05	6
Recommended	*0.28*			*0.12*		
Published Range	*0.21 to 0.48*		*7*	*0.10 to 0.15*		*5*
BIR-1	0.27	0.04	3	-0.02	0.05	3
Recommended	*0.26*			*0.02*		
Published Range	*0.20 to 0.36*		*5*	*-0.02 to 0.08*		*3*
Nod P1	0.86	0.06	3	0.28	0.09	3
Published Range	*0.78 to 0.87*		*3*	*0.29 to 0.46*		*3*
BCR-2	0.33	0.06	3	nd		
Recommended*	*0.25*			*0.17*		
Published Range*	*0.20 to 0.33*		*12*	*0.07 to 0.22*		*6*

* Combined BCR1/2

'n' refers to the number of complete duplicates analysed in this study, or the number of studies compiled in the given published range.

Table 2

Table 2. Data table, including calculated CIA and IOL values (see text for details), S concentrations, calculated τ values (where j = Nb, and p = SQ2-6 mean: see Eqn. 5 and text for details), measured Zn and Cu isotope values, and calculated Δ isotope values (where $\Delta = \delta_{sample} - \delta_{SQ2}$). Fe_2O_3 and MnO concentrations from Wimpenny et al. (2007). Li, Zn and Cu concentrations from Howarth et al. (2018).

| Zone	Sample	Depth m	ρ gcm^{-3}	CIA	IOL	S μg/g	Fe_2O_3 wt%	MnO wt%	Li μg/g	Zn μg/g	Cu μg/g	$\tau_{Fe,Nb}$	$\tau_{Mn,Nb}$	$\tau_{Li,Nb}$	$\tau_{Zn,Nb}$	$\tau_{Cu,Nb}$	$\delta^{66}Zn$ ‰	2 SD	$\Delta^{66}Zn$ ‰	$\delta^{65}Cu$ ‰	2 SD	$\Delta^{65}Cu$ ‰
IV	SQ14	0	1.45	97	86	350	48.5	0.04	8.8	31	61	2.7	-0.89	-0.88	-0.87	-0.52	-0.02	0.07	-0.51	-0.87	0.07	-0.89
	SQ13	2.5	1.57	97	82	418	45.0	0.04	9.5	25	50	2.9	-0.87	-0.85	-0.89	-0.56	nd	nd	na	-0.70	0.07	-0.73
	SQ12	3.5	1.64	98	80	274	36.4	0.06	7.1	25	39	1.6	-0.85	-0.91	-0.90	-0.71	0.07	0.07	-0.42	-0.69	0.07	-0.67
	SQ12dup																nd			-0.61	0.07	
III	SQ11	7.5	1.25	95	84	203	68.3	0.57	4.2	97	52	18.9	5.5	-0.78	0.51	0.54	0.14	0.07	-0.34	-0.30	0.07	-0.32
	SQ10	8.5	1.80	96	82	408	49.6	0.02	4.5	21	31	4.6	-0.91	-0.91	-0.87	-0.64	0.15	0.07	-0.33	-0.86	0.07	-0.89
II	SQ9	12	1.29	92	31	205	10.8	0.02	8.7	23	34	0.59	-0.91	-0.77	-0.82	-0.49	0.28	0.07	-0.20	-0.60	0.07	-0.63
	SQ8	13.5	1.37	92	31	227	10.3	0.02	9.7	38	38	0.37	-0.87	-0.77	-0.73	-0.48	0.02	0.07	-0.46	-0.45	0.07	-0.47
	SQ7	14	1.25	90	27	192	7.6	0.06	13.8	38	42	0.07	-0.64	-0.66	-0.72	-0.40	0.38	0.07	-0.11	-0.03	0.07	-0.06
I	SQ6	15	2.20	59	18	630	3.4	0.05	20.2	66	53	-0.26	-0.46	-0.22	-0.23	0.19	0.42	0.07	-0.06	-0.23	0.07	-0.25
	SQ5	22.5	1.99	63	27	861	7.6	0.17	45.0	146	37	0.44	0.59	0.51	0.47	-0.29	0.53	0.07	0.05	-0.28	0.07	-0.31
	SQ4	25.5	2.23	57	15	343	2.4	0.07	12.5	33	66	-0.20	0.01	-0.27	-0.43	1.24	0.43	0.07	-0.05	-0.05	0.07	-0.08
	SQ3	30	2.68	58	22	818	5.6	0.11	32.4	115	40	-0.12	-0.22	-0.10	-0.04	-0.36	0.47	0.07	-0.01	0.04	0.07	0.02
	SQ2	34	2.75	57	23	725	6.1	0.13	31.6	112	50	0.04	0.06	-0.04	0.02	-0.12	0.51	0.07	na	0.01	0.07	na
	SQ2dup																0.48	0.07		0.04	0.07	
Dyke	SQ1	-	3.11	-	-	1634	-	-	7.4	127	122			na	na	na	0.35	0.07	na	0.08	0.07	na
										Integrated (all):		1.5	0.02	-0.28	-0.23	-0.07			-0.14			-0.32
								Integrated (excl. zone III):				0.36	-0.21	-0.21	-0.22	-0.06			-0.11			-0.28

nd – not done

na – not applicable
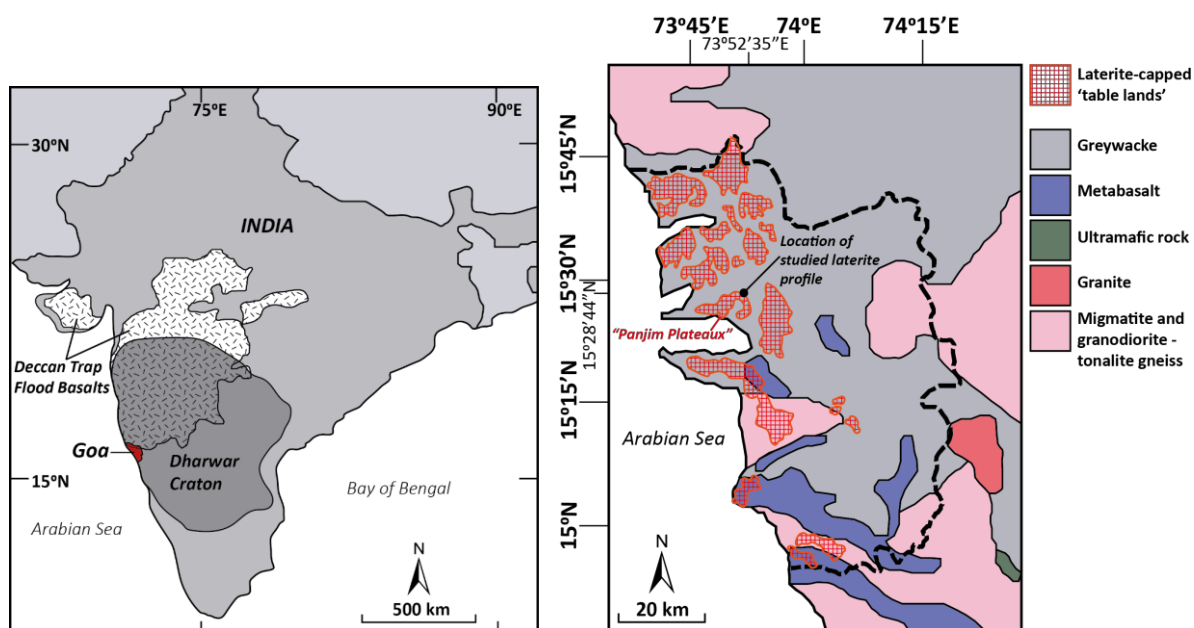
Figure 1. **Left**: The location of Goa state (red) on the Indian Dharwar Craton (adapted from Paton et al., 2007). In the northeastern corner of the state, Deccan Trap flood basalts overlie the Dharwar metasediments. **Right**: The geology of Goa state (adapted from Devaraju et al., 2010 and Widdowson, 2009). The black dashed line represents the state boundary. The Merces Quarry (SQ) laterite profile (labelled) is located at 15°28'44"N, 73°52'35"E. It is developed on Dharwar Late Archaean biotite-bearing greywacke.
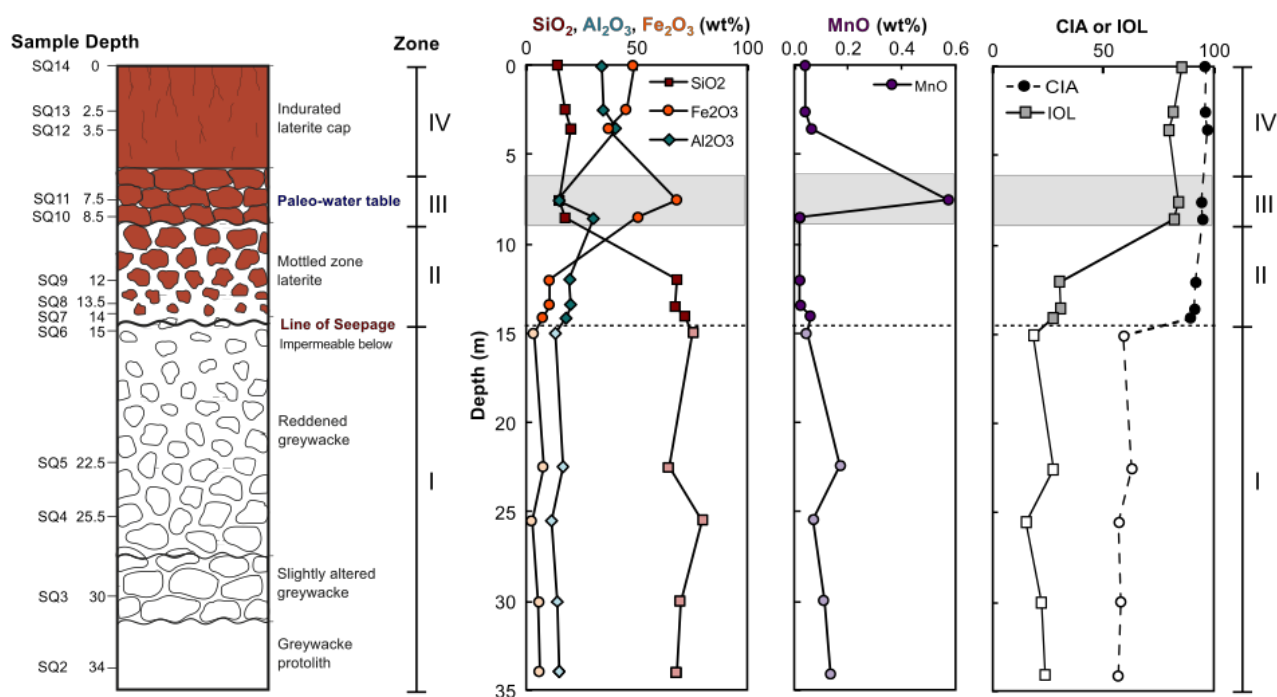
Figure 2. Left: Schematic illustrating the depth distribution of samples in the laterite profile in relation to characteristic zones of alteration (Wimpenny et al., 2007; Widdowson, 2009). Graphs from left to right: Major element concentration variations (SiO_2, Al_2O_3, Fe_2O_3; Widdowson, 2009), MnO concentration variations (Widdowson, 2009), and indices of alteration (Chemical Index of Alteration, CIA; Index of Lateritization, IOL; see text for further details). Grey shading highlights zone III, the paleo-water table. Samples showing only limited alteration, from below the dotted line of seepage (zone I), are paler in colour.
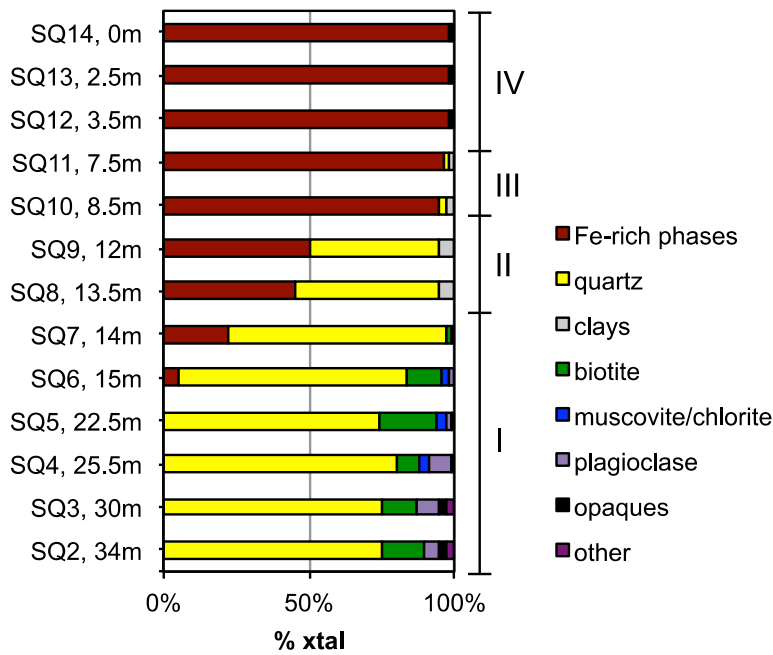
Figure 3. The crystal abundances of major mineral phases in the SQ laterite weathering profile compared to the four identified zones of alteration (see also Fig. 2; after Wimpenney et al., 2007).
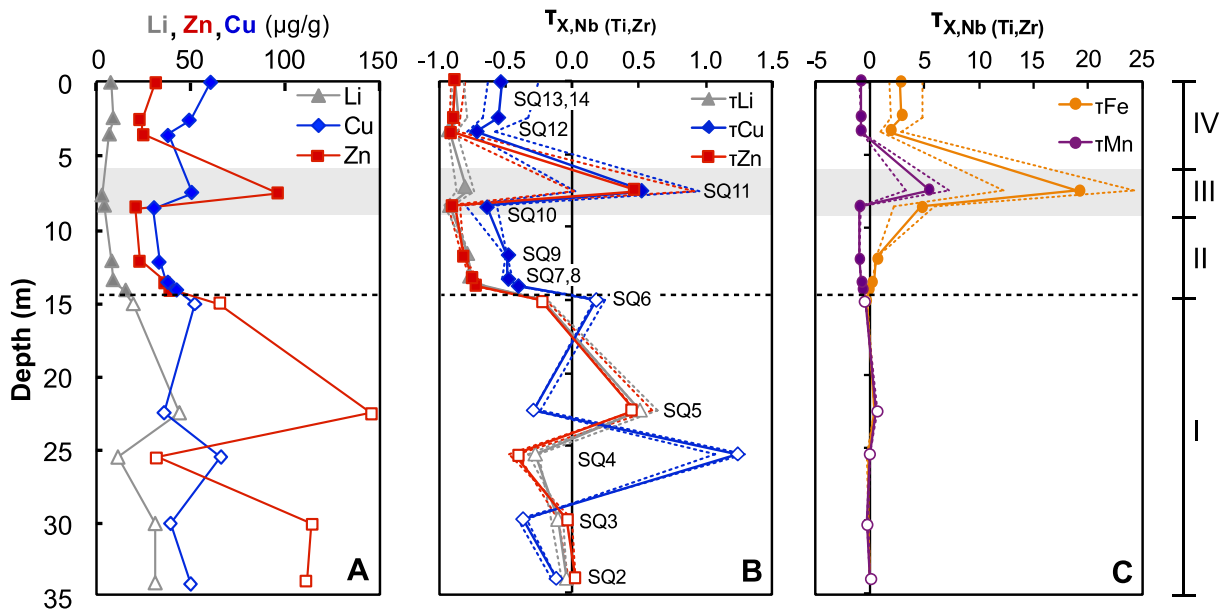

Figure 4. A. Concentration profiles and **B.** τ enrichment-depletion profiles (see text for details) of Li (grey triangles), Zn (red squares) and Cu (blue diamonds) in the SQ profile. **C.** τ enrichment-depletion profiles for Fe and Mn. Open symbols: little altered samples in zone I, below line of seepage (dotted line). Filled symbols: altered samples in zones II-IV, above line of seepage. Grey shaded zone III has been influenced by the paleo-water table.
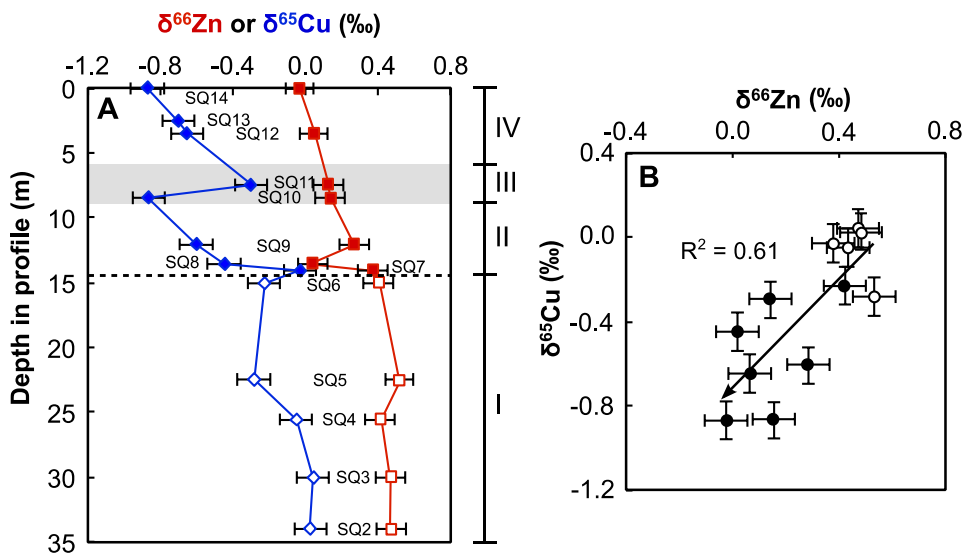
Figure 5. A. Depth profiles of $\delta^{66}Zn$ (red squares) and $\delta^{65}Cu$ (blue diamonds). Open symbols: unaltered-little altered samples in zone I, below line of seepage (dotted line). Filled symbols: increasingly altered zone II-IV mottled and lateritic samples. Shaded grey rectangle: zone III, influenced by the paleo-water table. **B**. Positive correlation between $\delta^{66}Zn$ and $\delta^{65}Cu$ in the SQ profile. Linear regression (arrow) indicates coupled loss of heavy Cu and Zn isotopes during lateritization and a resultant shift towards residual isotopically light values. Error bars represent long-term external 2SD reproducibility.
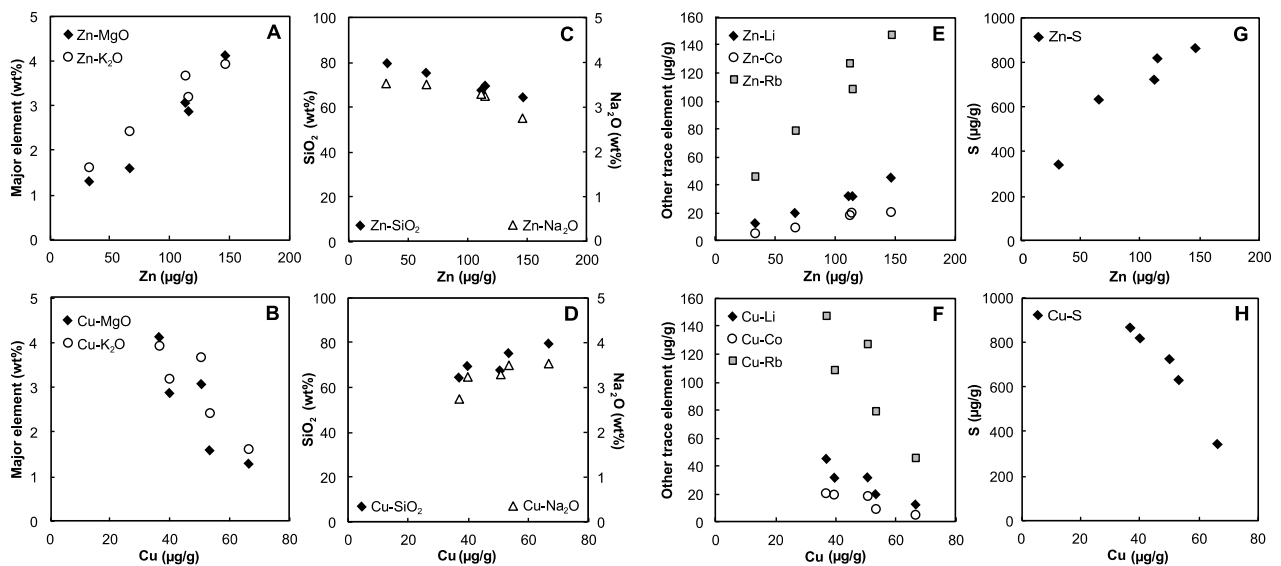

Figure 6. Covariation of Zn and Cu with selected major (A-D) and trace elements (E-H) in samples from zone I (unaltered – little altered) of the SQ laterite profile. Positive correlations of Zn with elements commonly hosted in biotite (Mg, K, Li, Co and Rb) suggest that Zn is primarily hosted in biotite in the parent greywacke (see also Fig. S3). Copper shows negative correlations with most other major and trace elements, with the exception of SiO_2 and Na_2O (Panel D), suggesting an association with a detrital phase.
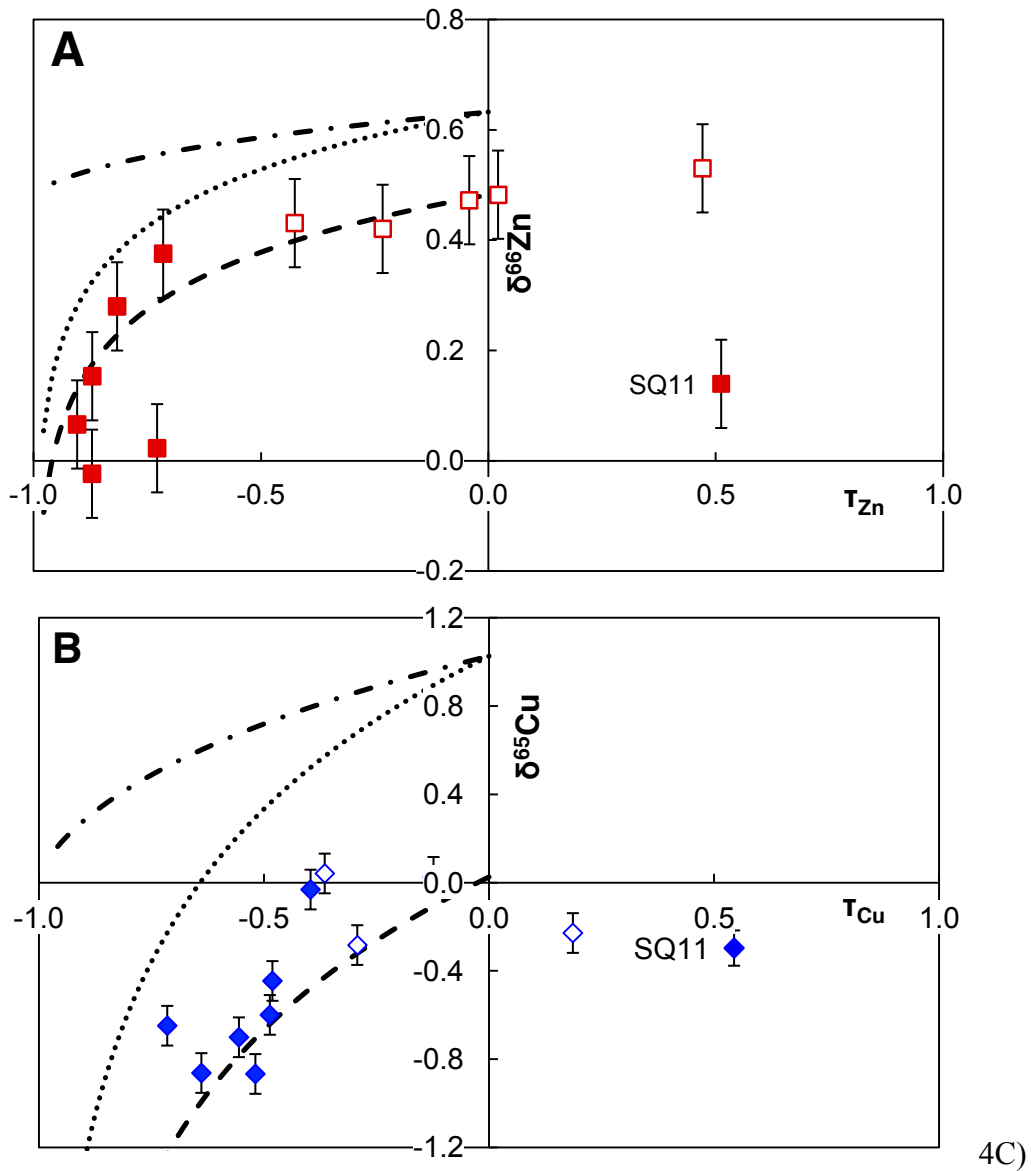
Figure 7. Rayleigh fractionation modelling of **A**. Zn and **B**. Cu isotopes assuming preferential mobilization of heavy isotopes to the dissolved phase, assuming $R = R_0 \cdot f^{\alpha-1}$ (where R_0 is the isotope ratio of the protolith (larger open symbols), f the fraction removed and α the fractionation factor. For Zn: $\alpha = 1.00015$, for Cu: $\alpha = 1.001$). Dashed line: residual isotopic composition of the solid. Dash-dotted line: cumulative isotopic composition of the fluid removed from the system. Dotted line: instantaneous fluid isotopic composition. Symbols as in Figures 4 and 5. Error bars represent long-term external 2SD reproducibility. Paleo-water table sample SQ11 labelled.
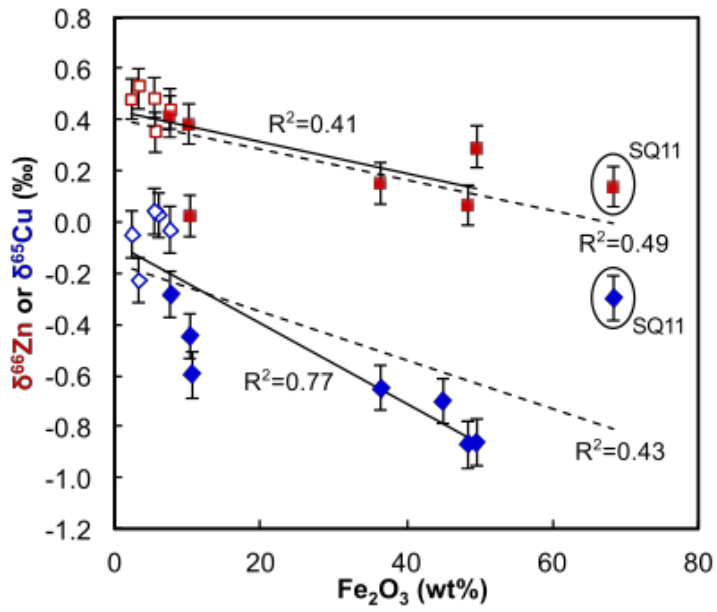
Figure 8. Negative correlations of δ^{66}Zn (red squares) and δ^{65}Cu (blue diamonds) with Fe_2O_3 in the SQ profile. Paleo-water table sample SQ11 is circled, other symbols as in Figure 5. Regressions are shown excluding (solid lines) and including (dashed lines) SQ11. Error bars represent long-term external 2SD reproducibility.
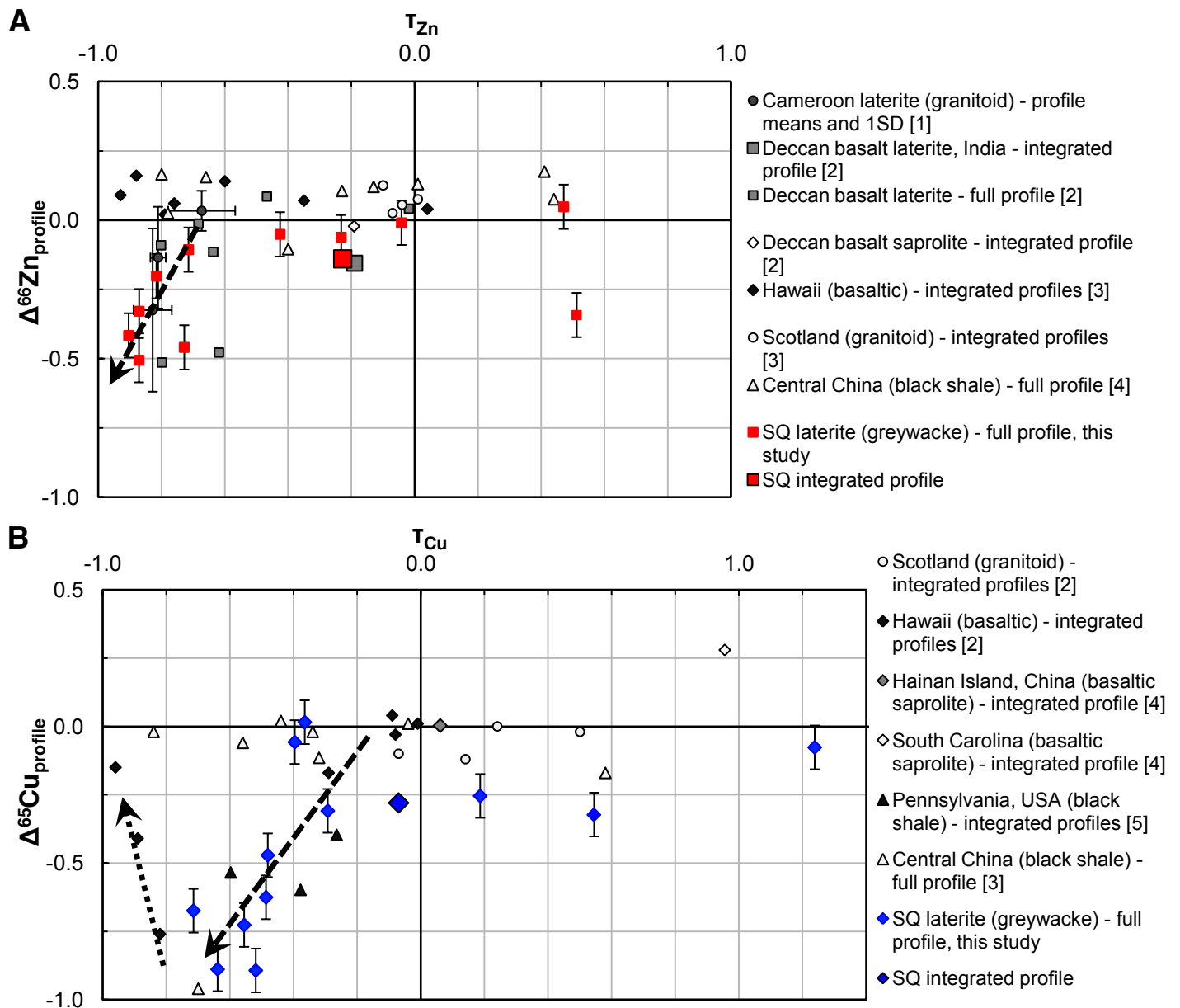
Figure 9. Integrated τ and integrated isotopic compositions for global soils **A**. Zn and **B**. Cu. Note, data are only included for studies where τ values are reported or can be calculated (Viers et al., 2007; Mathur et al., 2012; Liu et al., 2014; Lv et al., 2016; Vance et al., 2016). In order to include as much data as possible, but where an integrated τ-value cannot be calculated because horizon depths are not reported, either the full soil profile (for the central China black shale; Lv et al., 2016) or the mean and 1SD for each published profile (for the Cameroon laterite profiles; Viers et al., 2007) is shown. The SQ laterite dataset is shown as a full profile and as an integrated signature (larger symbol). Recently published full profile Zn isotope data is also included for the Bidar laterite, developed on Deccan basalt, for comparison (Zn only: Suhr et al., 2018). Literature data: [1] Viers et al. (2007), [2] Suhr et al. (2018) [3] Vance et al. (2016), [4] Lv et al. (2016), [5] Liu et al. (2014), [6] Mathur et al. (2012).